Computational Fluid Dynamics for the Design of Efficient Cell Seeding Device

A Thesis Presented

by

Adebayo Adeniran Adebiyi

to

The Department of Mechanical and Industrial Engineering

in partial fulfillment of the requirements for the degree of

Master of Science

in

Mechanical Engineering

Northeastern University

Boston, Massachusetts

April 2011

ABSTRACT

The seeding of a porous scaffold with stem cells is a fundamental step in engineering sizeable tissue constructs that are clinically viable. However, a key problem often encountered is inhomogeneous seeding of the cells particularly when the cells are delivered through the thickness of the scaffold. To address this problem, different seeding techniques and technology have been investigated. Though few studies have employed computational modeling to theoretically evaluate and characterize available seeding techniques and technology, a transient computational fluid dynamics (CFD) quantification and optimization of an existing clinically viable seeding technique and technology has yet to be reported. The objective of this study was to establish the quantitative relationships between the cell seeding efficiency and the initial vacuum pressure in a compact perfusion seeding device that uses the effect of differential pressure induced by vacuum to seed cells on a porous scaffold. Since fluid flow provides an ideal means of transporting the cells into the scaffold, transient CFD solution of the fluid flow in the cubic configuration of the device was obtained using the initial vacuum pressure recommended in the patent for the device. Subsequently, the initial vacuum pressure was optimized for efficient cell seeding and applied to a cylindrical configuration of the device. Results indicate that the optimal initial vacuum pressure for homogenous cell seeding is approximately -20kPa for both configuration of the seeding device. This optimal initial vacuum pressure is approximately 80% lower than recommended in the patent. This study presents a 3-D computational model that can be employed as part of a systemic stepwise approach to designing and optimizing cell seeding techniques and corresponding technology.

ACKNOWLEDGEMENTS

I give all glory to God who by His mercy and grace has enabled me to start and complete my graduate degree program.

My gratitude goes to my advisor Professor Mohammad Taslim for the help, valuable suggestions and encouragement provided while carrying out this research.

I am deeply indebted to my mentors; Dr. Keith Crawford and Dr. Sheila Nutt for encouraging me to further my education and their support while in graduate school.

I thank my guardian, Mr. Ayo-Yakubu and Mrs. Bolade Owolewa, for their numerous words of encouragement and contributions toward the success of my education.

Lastly, and most importantly, I thank my loving parents, Mr. Jacob Adebiyi and Mrs. Felicia Bolanle Adebiyi for their unlimited moral and financial support. To them I dedicate this thesis.

TABLE OF CONTENTS

Chapter **Page**

Chapter **Page**

NOMENCLATURE

Δp	pressure drop
$\vec{v}$	velocity field
α	permeability
$\vec{v}_s$	the velocity field for the secondary phase
ρ_s	density of the secondary phase
$\dot{m}_{ps}$	the mass transfer from the primary phase (air) to the secondary phase
$\dot{m}_{sp}$	the mass transfer from the secondary phase to the primary phase
S_{α_s}	source term (zero by default)
α_s	secondary phase volume fraction
α_p	primary phase volume fraction
$n+1$	index for current time step
n	index for previous time step
$m+1$	index for current iteration
m	index for previous iteration
$\alpha_{s,f}$	face value of the secondary phase volume fraction, CICSAM
V	volume of cell
U_f	volume flux through the face, based on normal velocity
P	static pressure
μ	is the molecular viscosity
$\rho\vec{g}$	gravitational force
$\vec{F}$	external body force
$a_p(\boldsymbol{u}^{(m)})$	coefficient function of $\boldsymbol{u}^{(m)}$
$a_{l,p}(\boldsymbol{u}^{(m)})$	coefficient function of $\boldsymbol{u}^{(m)}$ in neighboring nodes

$Q_p(\boldsymbol{u}^{(m)})$	source consisting of the body force and other terms
$u^*_{i,p}$	velocity component at grid point p
$u^*_{i,l}$	velocity component of neighboring nodes
u_i'	velocity component correction
p'	pressure correction
$\left(\frac{\delta p}{\delta x_i}\right)_p$	discretized pressure partial derivatives at grid point p
$\boldsymbol{u}$	fluid velocity vector
$\boldsymbol{u}_p$	particle velocity vector
ρ	fluid density
ρ_p	particle density
d_p	particle diameter
m_p	particle mass
$\boldsymbol{F}_{drag}$	particle drag force
$\boldsymbol{F}_{gravity}$	particle buoyancy force
$\boldsymbol{F}_{pressure}$	particle pressure force
$\boldsymbol{F}_{virtual\ mass}$	particle virtual mass force
$\boldsymbol{F}_{other}$	other forces on particle

LIST OF TABLES

LIST OF FIGURES

Figure **Page**

Figure **Page**

INTRODUCTION

1.1 Tissue Engineering

Tissue engineering is an interdisciplinary field that applies the principle of engineering and the life sciences to the development of biological substitutes that restores, maintain, or improve tissue function [1]. A study by Bisceglie in 1930 was the first attempt to demonstrate that engineering tissue is possible. In this study, he encased mouse tumor cells in a polymer membrane and inserted them into pig's abdominal cavity. Results from this study provided evidence that cells could survive and not be destroyed by the immune system [2]. Furthermore, in 1972, Knazek et al. successfully cultured cells from established lines on bundles of artificial plastic capillaries [3]. Based on the results from these two studies, Chick et al. in 1975 was able to develop a prototype for an artificial endocrine pancreas in a rat model. Here, Chick and co-workers cultured beta cell on synthetic capillaries unit. This unit consisted of silicon polycarbonate capillaries mixed with Amicon XM-50 fibers. Data obtained from this study indicated that the beta cells cultured on the artificial capillary unit continued to synthesize, store, and release insulin [4].

With further advances in the field of tissue engineering, Bell et al. in 1981 successfully grafted living skin-equivalent grafts on an open wound made on the back of a rat model. These grafts consisted of fibroblasts isolated from a skin biopsy from a rat donor cast in lattice obtained from rat collagen and seeded with epidermal cells [5]. In a similar study, Burke et al. created a biodegradable scaffold composed of a bilayer membrane with anatomic structure and chemical composition that closely resembles dermis and able to induce synthesis of a neodermis. This membrane consisted of a distinct epidermal and dermal portion. The dermal portion was made

from bovine hide collagen and chondroitin 6- sulphate obtained from shark cartilage. The epidermal portion composed of a homogeneous layer of medical grade silastic. This biodegradable scaffold was later used as a model for the synthesis of an artificial skin to physiologically close up 60% of the body surface of burn wounds in ten patients with total burn size covering 50 – 90% of their body surface area [6].

Motivated by these studies, Vacanti et al. successfully attached cells from liver, intestine, and pancreas to an artificial biodegradable polymer of polyglactin 910, polyanhydrides, and polyorthoester [7]. In the following years, researchers focused on developing artificial biodegradable scaffold that allows the physical and biological properties to be modified.

1.2 Tissue Engineering Scaffolds

Scaffolds can be seen as 3-D supporting structures that mimic the function of the natural extracellular matrix and provide temporary mechanical support for cells to attach, proliferate and maintain their differentiated function [8]. Scaffolds play a key role in tissue engineering. Potential use of a material as scaffold in tissue engineering depends primarily on the structure and the characteristic of the material. Desirable features for any scaffold material would include biocompatibility, degradability, high porosity and interconnectivity. Many natural and synthetic scaffold materials have been investigated for tissue engineering applications. Some of the natural polymers are collagen and chitin. Other artificial polymers include hdroxyapatite (HA), poly (α-hydroxyester), polyglycolide (PGA), polyactides (PLLA, PDLA), polycaprolactone (PCL) etc. In some cases the natural polymers are blended with the artificial polymers.

1.3 Motivation of Research

The ultimate goal of tissue engineering is the application of principles and methods of engineering and life sciences to engineer 3D tissues by bringing scaffold and cells together to form adequate and functional tissues and organs that can be used to repair, replace or/ and regenerate lost or damaged tissues and organs.[9,10,11]. As stated by Langer et al. in an excellent paper, up to 8 million surgical procedures are performed annually in the United States to treat patients suffering from tissue loss or organ failure. These procedures require about 40 – 90 million hospital days [11]. The total US health care cost to treat these patients was reported to exceed $400 billion annually. Additionally, the total market for tissue-engineered products in the United States is estimated to be $80 billion annually [1]. Moreover, Griffith et al. recently envisioned that *in vitro* or *ex vivo* engineered 3D tissues can potentially be used as an external organ support devices when a compatible donor is not available as well as a model systems in drug screening [12, 13]. It is noteworthy, however, that the process of engineering 3D tissue construct has proven to be challenging because the parameters enabling the success of the process are not clearly understood [14].Consequently, comprehensive multidisciplinary research to address these challenges is imperative. In this regard, improving and optimizing processes key in engineering 3D tissue construct starting with cell source, cell selection, *in vitro* cell expansion, scaffold design, cell seeding on porous scaffold, nutrition of cells in the resulting construct and mechanical stimulation of the developing tissue has been the focus of researchers over the past few years [8, 15, 16, 17, 18, 19].

1.4 Advances in Tissue Engineering

Many publications have been issued on the subject of tissue engineering. Some of these studies focused on the design and optimization of scaffolds. Other studies focused on improving cell seeding techniques and efficiency. Additionally, some studies were performed on understanding the process of mecahnostimulation of cells and bioreactor cultivation. In one of these studies, the scaffold pore morphology was reported to have significant influence on the tissue regeneration process [8]. In other studies, it was identified that the culture medium flow rate and the scaffold 3D geometry and micro-architecture influence fluid flow stimulation of cells attached to the scaffold [20, 21, 22]. A few studies on cell seeding efficiency reported that the initial distribution of cells within the scaffold after seeding is related to the distribution of tissue subsequently formed with the engineered construct [23, 24, 25, 26]. Martin et al. in a review paper reported that seeding cells into scaffolds at high densities enhance tissue formation in 3D constructs, including high rates of cartilage matrix production [27], increased bone mineralization [23] and enhanced cardiac tissue structure [28]. Taken together, it is important to design functional scaffolds with architecture that is able to provide uniform mechanical stimuli to the cells and temporary mechanical support for tissue regeneration; seeding devices that permits cell seeding techniques that can produce homogeneous cell distribution within the scaffold; and bioreactors with automated and controlled procedures that promotes the manufacture of reproducible and reliable engineered tissue complying with good manufacturing practice requirements [29, 30].

1.5 Cell seeding for tissue engineering

Cell seeding is the process of incorporating cells into or unto the scaffold prior to culture or implantation. Soletti et al. reported that the process of cell seeding is a fundamental step in tissue engineering applications. An efficient seeding technique will minimize cell injury, reduce cell seeding time, seed cells uniformly on the scaffold, be highly reproducible and be user independent [31]. However, the use of cell seeding devices has proven to be challenging because it involves mechanical forces that may result in shear-mediated lysis or triggering apoptotic pathways [32, 33]. Cells can be seeded on the scaffold by lining the cells on the surface of the scaffold (surface seeding) or by delivering the cells through the thickness of the scaffold (bulk seeding). Surface seeding is by far the most commonly used seeding method since bulk seeding is difficult to achieve in a controllable manner. In one of the most common bulk seeding approaches, cells are dripped in the scaffold matrix. However, this technique does not produce a high yield of cells in the scaffold. In addition, the manual nature of this process does not permit quality control on the final engineered tissue [34, 35]. Martin et al. in a review paper reported various methods of cell seeding namely; static, stirred flask and perfusion method [36]. In Static method the cells are spread on the surface of the scaffold with the aid of a micropipette. This method can readily be used for any cell type and scaffold configuration. However, many studies have reported low seeding efficiencies [23, 26, 37, 38, 39]. In the stirred flask method, scaffolds are suspended in a well mixed spinner flask filled with the cell suspension. The mixing provides a relative velocity between the suspended cells and the scaffold (Figure 1.5.1). Thus, the cells are transported to and into the scaffold by convection [26, 28, 40, 41, 42]. A key problem often

encountered in stirred flask cell seeding is non-uniform distributions of cells with a higher density of the cells lining the scaffold surface.

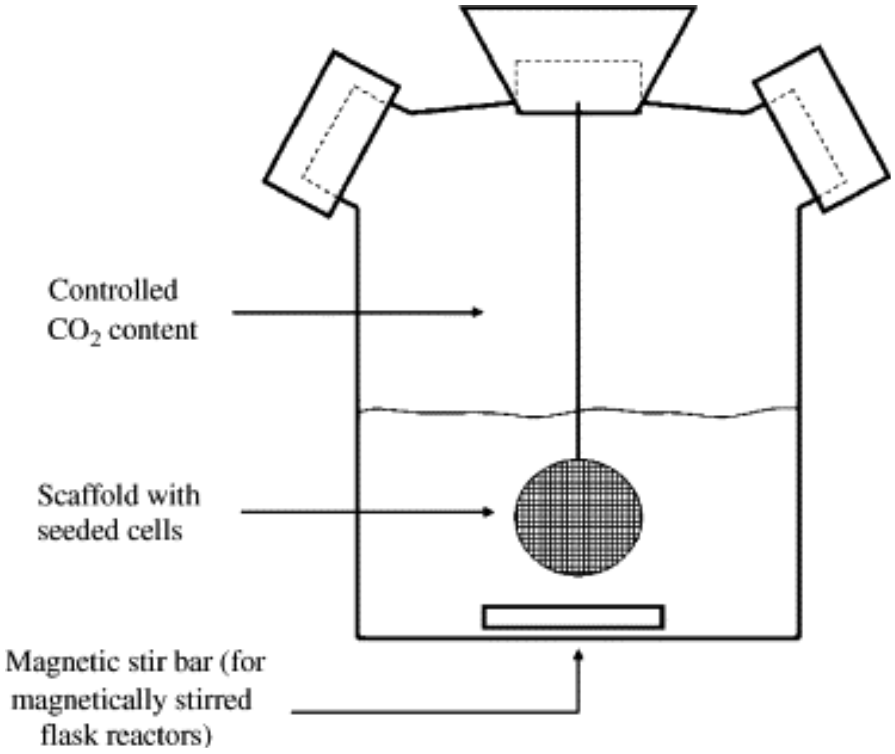

Figure 1.5.1: Sample stirred flask seeding device for tissue engineering.

(Courtesy: Martin Y, Vermette P. 2005. Bioreactors fortissue mass culture: Design, characterization, and recent advances. Biomaterials26(35):7481-7503)

For the direct perfusion method, the cells suspension flows directly through the scaffold thus depositing cells directly into the scaffold pores (Figure 1.5.2). Comparison of these three methods suggested that, the direct perfusion method produced the highest seeding efficiency [42]. It is therefore worthwhile to pursue further advances in the direct perfusion method of seeding.

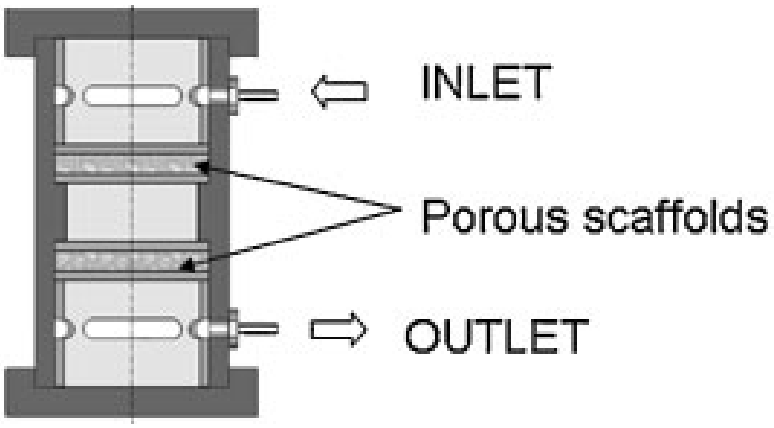

Figure 1.5.2: Sample perfusion seeding bioreactors for tissue engineering.

(Courtesy: Raimondi MT, Boschetti F, Falcone L, Migliavacca F, Remuzzi A, Dubini G.2004. The effect of media perfusion on three-dimensional cultures of human chondrocytes: Integration of experimental and computationalapproaches. Biorheology 41(3–4):401–410.)

1.6 Other examples of perfusion seeding devices

Over the past few years, different perfusion seeding devices have been designed by researchers. As a fundamental element, these devices are designed to better exploit the improved cell suspension transport into the scaffold obtainable in the perfusion technique. Wendt et al. [42] employed the use of oscillatory motion of fluid in a U-shaped tube to force the medium with the cell suspension through the scaffold (figure 1.6.1).

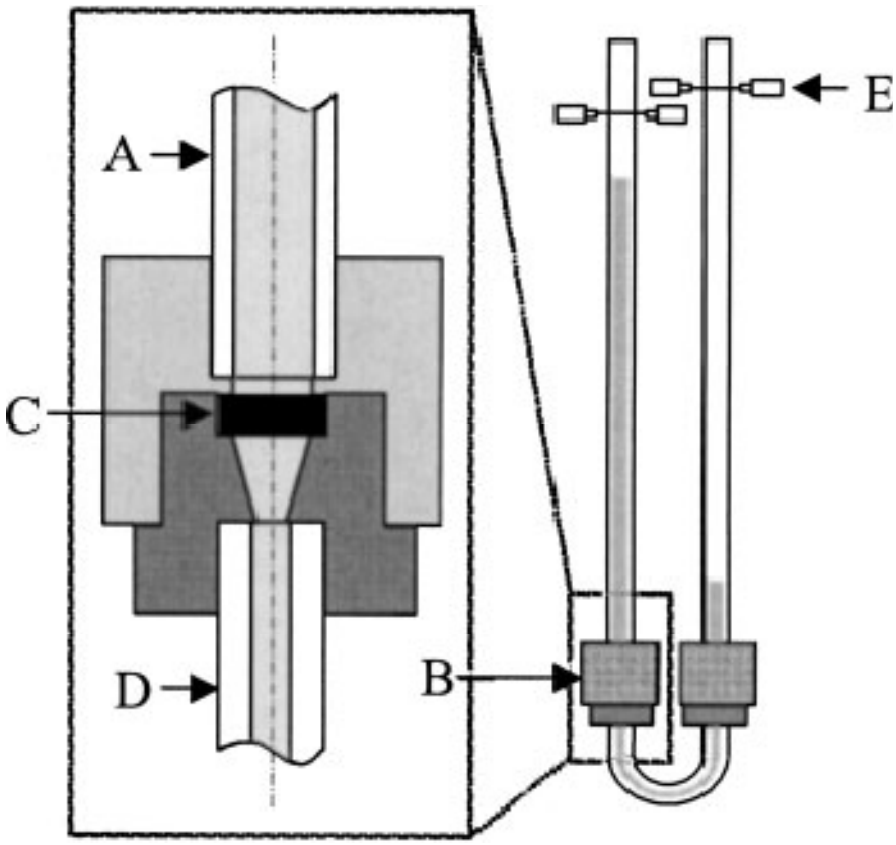

Figure 1.6.1: Sample perfusion seeding bioreactors for tissue engineering.

(Courtesy: Wendt, D., A. Marsano, et al. (2003). "Oscillating perfusion of cell suspensions through three-dimensional scaffolds enhances cell seeding efficiency and uniformity." Biotechnol Bioeng 84(2): 205-14.)

Two scaffolds (C) where placed in chambers (B) that were attached to the bottom of two vertical columns (A). The bottoms of the columns were connected with a U-tube (D) and the flow of the media was induced with the use of a vacuum pump. The vacuum is switched between the two columns in other to reverse the flow when the fluid reaches an optical sensor (E) placed near the top of each column.

In another approach, Soletti et al. [31] developed a seeding device that uses the synergistic effects of vacuum, centrifugal force and fluid flow to seed the scaffold (figure 1.6.2). The assembly is made up of an air-tight chamber that holds two rotating tees. These tees were connected to a precision syringe pump outside the chamber through hydraulic rotating joints and polyvinyl chloride (PVC) tubing. The scaffold to be seeded is mounted onto the tees. The flow of the cell suspension through the thickness of the scaffold is induced by the vacuum in the chamber. During this process the cells are entrapped in the pores of the scaffold while the fluid phase passes gradually out of the surface of the scaffold. The scaffold is continuously rotated during seeding to promote uniform circumferential seeding distribution.

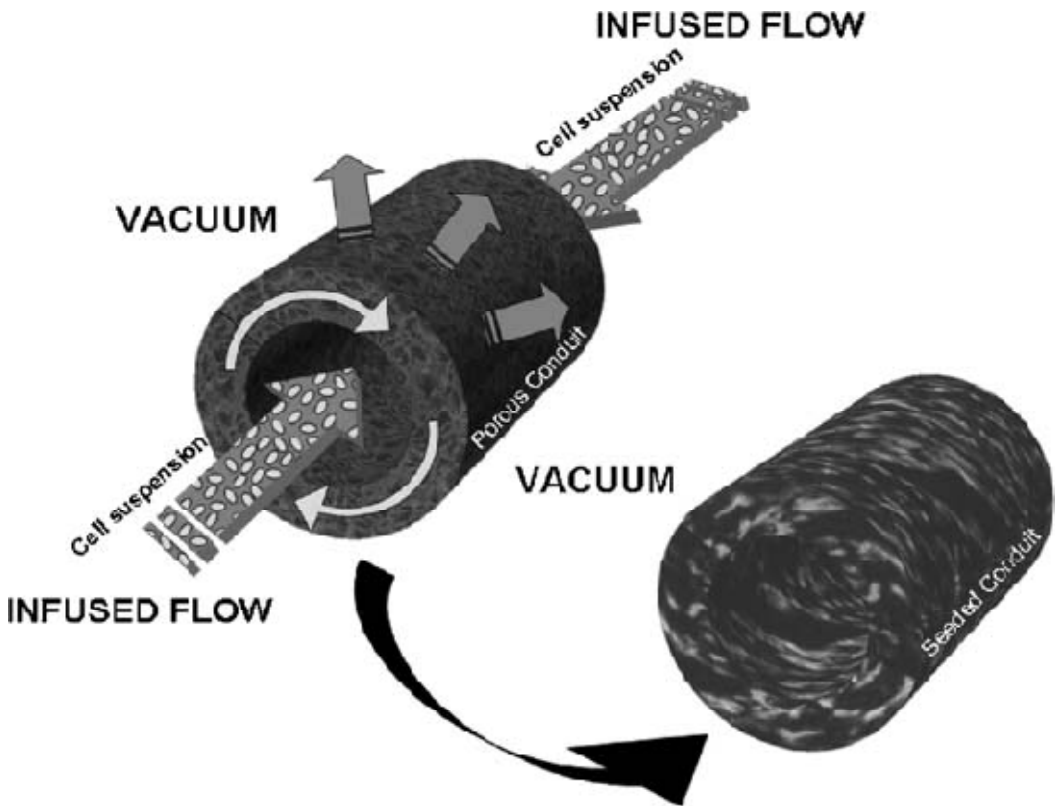

Figure 1.6.2: Sample perfusion seeding bioreactors for tissue engineering.

(Courtesy: Soletti, L., A. Nieponice, et al. (2006). "A seeding device for tissue engineered tubular structures." Biomaterials 27(28): 4863-70.)

1.7 Computational Fluid Dynamics and Modeling

Computational fluid dynamics (CFD) is a set of numerical methods applied to obtain approximate solutions to problems of fluid dynamics, heat and mass transfer. For instance, CFD methods are able to solve the Navier-Stokes equation to determine entire fluid flow fields such as velocity, pressure, density, temperature etc. CFD methods are very attractive because of the level of details they provide in addition to the fact that they allow the visualization of physical phenomena (e.g. fluid flow) often when it is impractical to position probes within the physical domain for measurement of parameters such as; velocity, temperature, pressure etc. However, a key problem often encountered is the increased complexity of the associated governing equations. In most cases, these equations are partial differential equations, often nonlinear. Nevertheless, an important benefit of CFD methods is the ability to evaluate far more design alternatives without having to perform numerous and expensive experiments. This benefit far outweighs the challenges often encountered in numerical methods. It is important to note that the CFD models are to be validated with experimental techniques.

1.8 Application of Computational Fluid Dynamics to Cell Seeding

Although, CFD methods has been predominantly used to model mechanical and chemical engineering flow and heat transfer problems, over the past few years, CFD simulations have found wide application in tissue engineering. For example, CFD simulations has successfully been used to quantify shear stresses acting inside microstructures [43, 44, 45].In another example, CFD simulations were used to numerically characterize fluid flow within a spinner flask under operating conditions used in cartilage tissue engineering [46]. Similarly, several

groups have used computational simulations to demonstrate how scaffold morphology influences hydrodynamic shear stresses and nutrients concentration restriction imposed in cells within construct [47]. Hence, CFD simulations has become a tool for tissue engineers to understand the influence of fluid flow and transport on cell function without having to perform many and expensive bioreactor experiments. Consequently, CFD simulation provides significant insight into the design and optimization of cell seeding devices while simultaneously saving time and resources.

1.9 Aim of Research Project and Specific Goals of This Thesis

A key problem, often encountered in tissue engineering of sizable construct is an inhomogeneous loading or seeding of cells on scaffold. Various studies have demonstrated that effective and homogeneous cell seeding into natural and synthetic scaffold is essential for developing functional tissue equivalent. In recent years, researchers have used computational fluid dynamics to characterize 3-D flows in tissue engineering bioreactors with different configurations. CFD modeling provides a detailed, efficient and nondestructive tool to theoretically evaluate and characterize large numbers of parameters that influence cells, tissue and organ in the context of tissue engineering without having to perform numerous experiments. It is noteworthy, however, that little work has been done in applying CFD modeling to design and optimize cell seeding techniques and devices in tissue engineering. Till now, a transient CFD simulation of a seeding technique and device that allows the manufacture of reproducible and reliable engineered constructs and able to reach general clinical application is lacking. The aim of this study was to introduce a time-dependent computational fluid dynamics model to characterize and optimize the mechanism of cell seeding in a compact perfusion seeding device that uses the effect of

differential pressure induced by vacuum to load early lineage adult (ELA) stem cells onto a demineralized bone matrix (DBM) scaffold. The immediate goals are:

Goal one: obtain the transient solution for fluid flow in the cubic configuration of the seeding device using an initial vacuum pressure in the range recommended in the patent (Govil et al. US Patent 2010/0155282 A1)

Goal two: determine the optimal initial vacuum pressure needed to homogeneously and effectively seed the scaffold with the cells by varying the vacuum pressure.

Goal three: develop a similar model for a cylindrical configuration of the seeding device using the determined optimal initial vacuum pressure.

MATERIALS AND METHODS

2.1 Design and Functional Principle of the Seeding Device

The seeding device is made up of an airtight cavity designed to hold the scaffold to be infused with the cell suspension. The cavity is made from polyvinylchloride (PVC) and may be cylindrical or cubic depending on the geometry of the scaffold. A support member is constructed to keep the cavity in a stable and upright position. The cavity is hermetically sealed by welding a top polystyrene web to its peripheral. A septum is places adjacent to the center of the cavity. To deliver the cell suspension into the cavity, a 20 gauge needle attached to a syringe containing the cell suspension is inserted into the entry port situated on the septum (figures 2.1.1, 2.1.2, 2.1.3)

The seeding device takes advantage of the vacuum induced suction effect and the corresponding pressure differential to initiate the flow of the cell suspension into the cavity. During this process, the cell suspension soaks the scaffold thereby depositing the cells uniformly in the scaffold. Capillary effect further aids the movement of the cells within the scaffold. The scaffold chamber is designed to promote a laminar flow down the side walls and on the bottom wall of the cavity to prevent clumping of cells together and forced apoptosis.

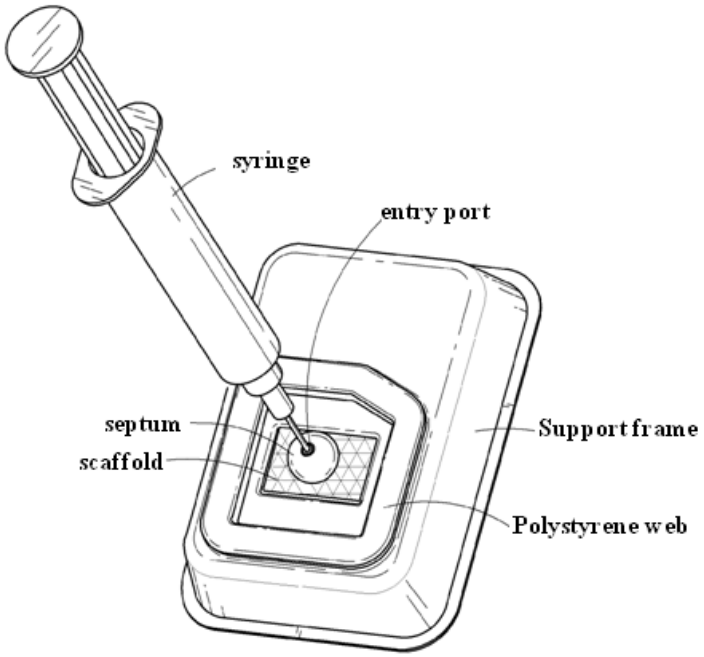

Figure 2.1.1: Seeding device for cubic scaffold

(Courtesy: Govil et al. US Patent 2010/0155282 A1)

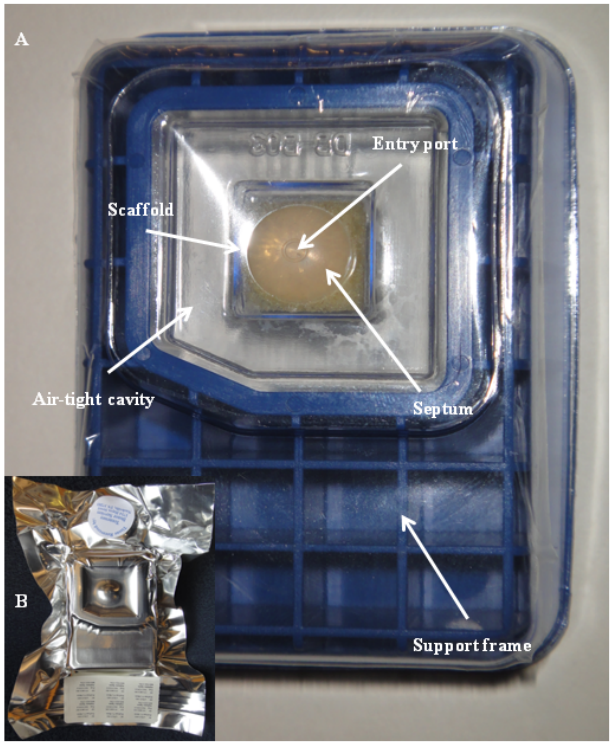

Figure 2.1.2: Alphatec^{TM} Spine technology (A) seeding device for the cubic scaffold (B) packaging

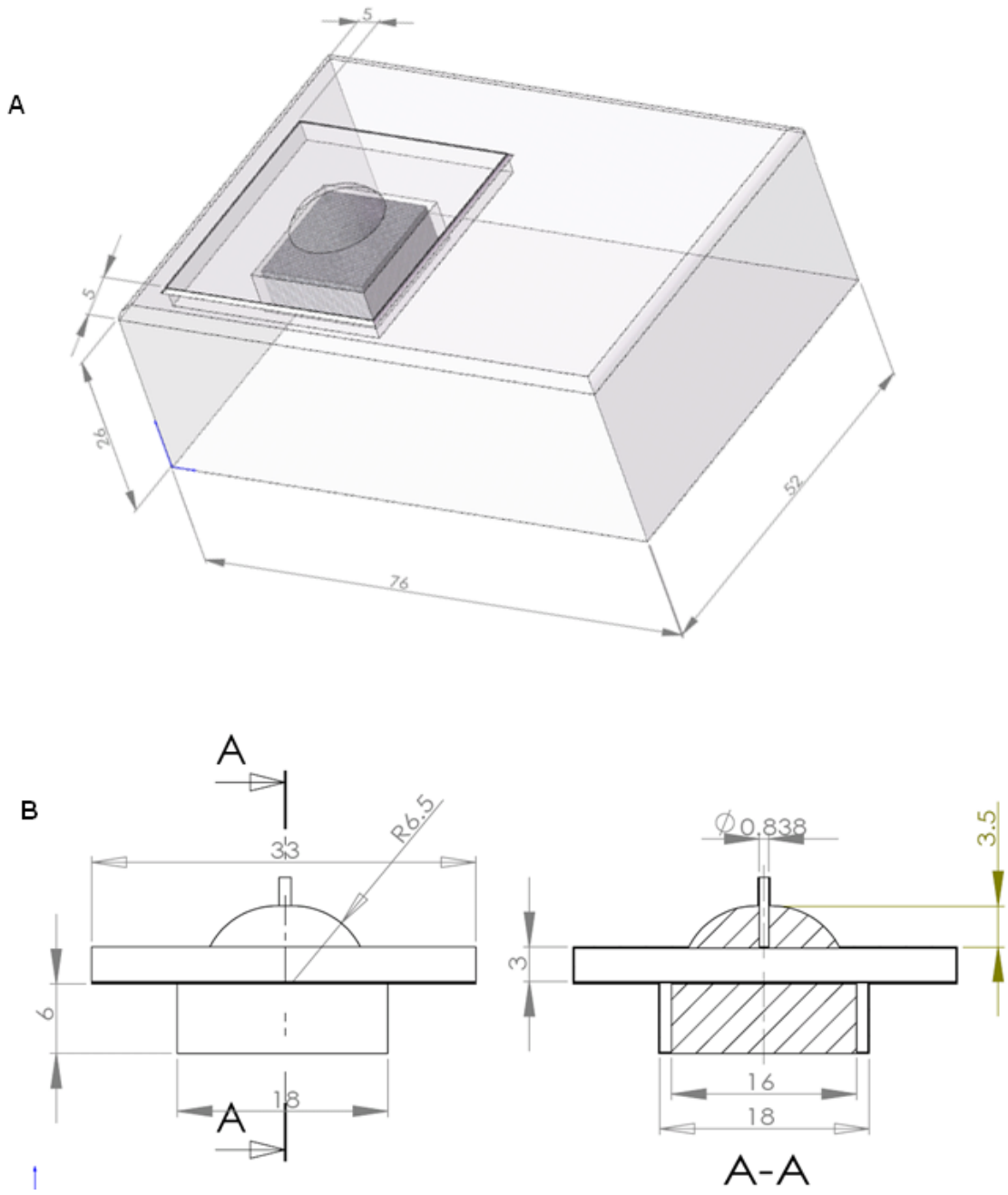

Figure 2.1.3: Schematics of seeding device showing major dimensions in millimeters

(A) modified seeding device for the cubic scaffold (B) working part with the tip of the needle piercing the septum

2.2 Scaffold

The scaffold is composed of Demineralized Bone Matrix (DBM) and is simulated as a porous medium with physical characteristics including a homogeneous porosity of about 80%, spherical pores of 598 ± 74.5 µm in diameter and a permeability coefficient in a magnitude of 10^{-8} to 10^{-14} m^2[48] .Two different geometries of scaffolds were used in this study. The first has a cylindrical geometry with a radius of 16mm and a height of 6mm and the second a cubic geometry with dimensions: 16 x 16 x 6 mm.

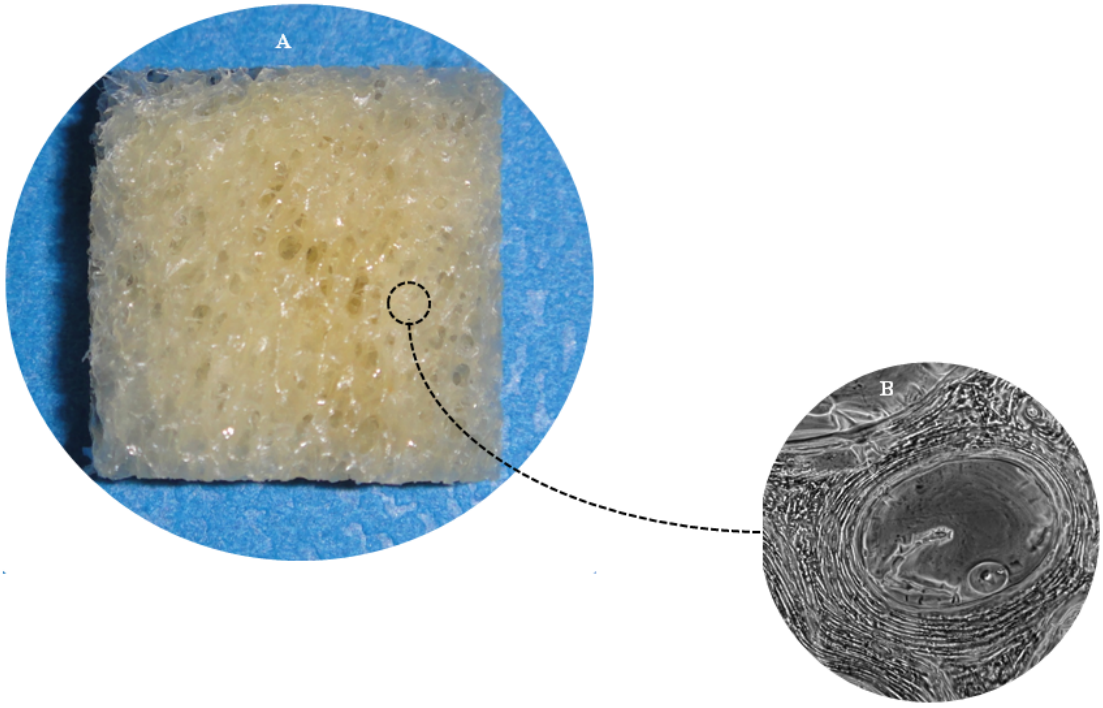

Figure 2.2.1: Demineralized bone matrix. (A) 16 x 16 x 6 mm DBM. (B) 10x image of a region of the scaffold showing details of a single pore

2.3 Mesh Generation

The computational fluid dynamics (CFD) software ANSYS FLUENT (version 12.0, ANSYS FLUENT, Lebanon, NH) was used to characterize the 3D flow of the cell suspension in the scaffold- cavity assembly. ANSYS FLUENT is a commercial CFD solver of partial differential equations (e.g. Navier-Stokes equation for fluid pattern analysis, Darcy's law for porous media, energy equation for heat transfer etc.) with attached physical and turbulence models, as well as modules for post-processing the results. To develop the model, two sets of meshes were generated. First, Hexahedral meshes containing 487,192 and 121,798 hexahedrons were created for the full (figure 2.3.1) and quarter (figure 2.3.2) geometry of the cubic scaffold- cavity construct respectively (Gambit 2.2 ANSYS FLUENT, Lebanon, NH). These meshes were created to investigate the presence of symmetry in the simulated flow field for the cubic scaffold-cavity assembly. The presence of symmetry will allow the use of a quarter section of the geometry as supposed to the full geometry. Hence, the computational time is significantly reduced and the computational cost is decreased without compromising the accuracy of the solution. Secondly, hexahedral mesh with boundaries containing approximately 435,000 and 489,000 hexahedrons was created for the quarter geometries of the cylindrical (Figure 2.3.3a) and cubic (figure 2.3.4a) scaffolds- cavity construct respectively. Furthermore, to perform grid independence check, hexahedral mesh containing 737,506 and 775,186 hexahedron was generated for the quarter geometries of the cylindrical (figure 2.3.4b) and cubic (figure 2.3.4b) scaffold– cavity construct respectively. Grid independence involves the generation of meshes of varying degrees of refinement, followed by their solution under similar or identical condition [47]. Following this, the solutions are compared for consistency in order to counter-check for the overall correctness of the simulation.

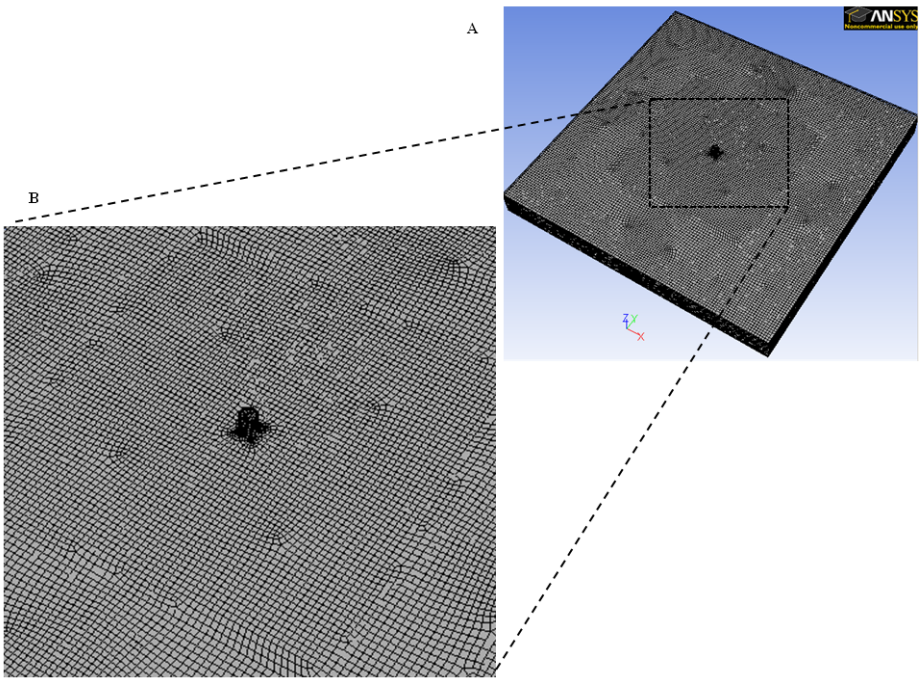

Figure 2.3.1: Full geometry (A) Hexahedral mesh of full scaffold-cavity assembly details (B) mesh around the tip of the needle

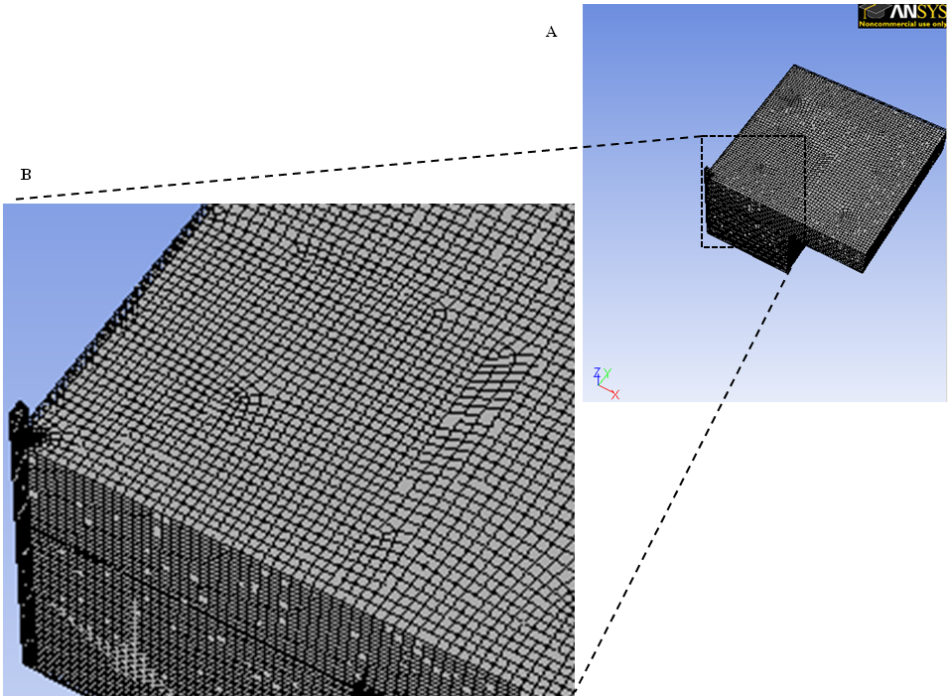

Figure 2.3.2: Quarter geometry (A) Hexahedral mesh of quarter section of scaffold-cavity assembly details (B) mesh around the tip of the needle

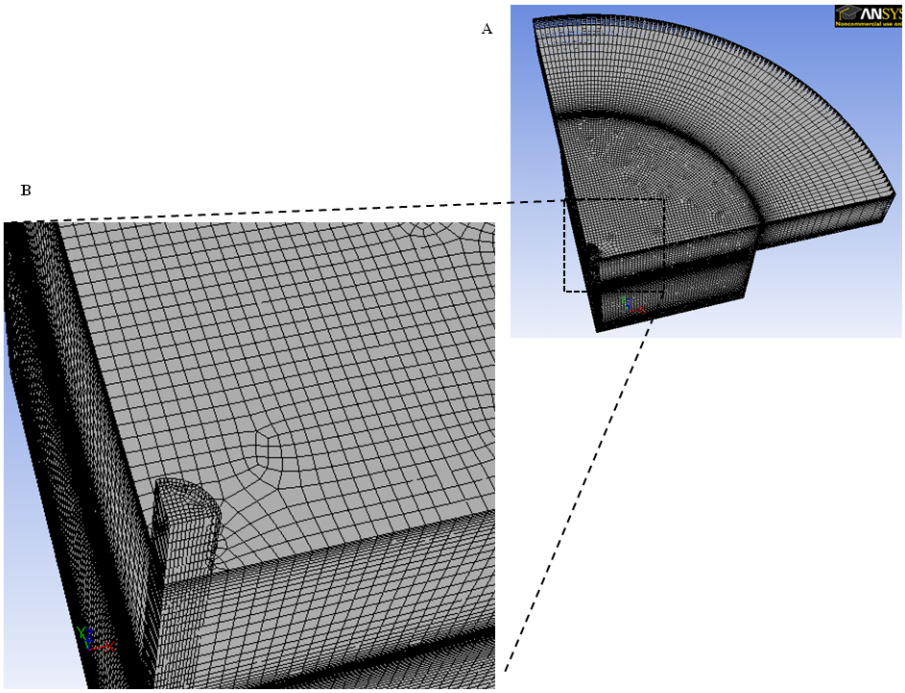

Figure 2.3.3a: Cylindrical configuration. (A) Hexahedral mesh of quarter section of cylindrical scaffold-cavity assembly with boundary details (B) mesh around the tip of the needle

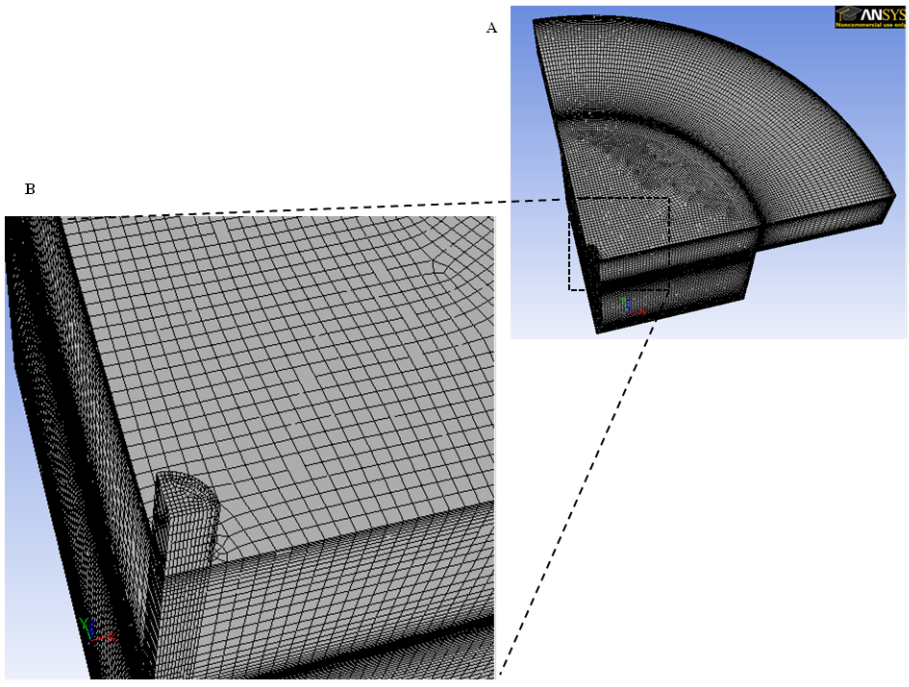

Figure 2.3.3b: Refined cylindrical configuration (A) Refined hexahedral mesh of quarter section of cylindrical scaffold-cavity assembly with boundary details (B) mesh around the tip of the needle

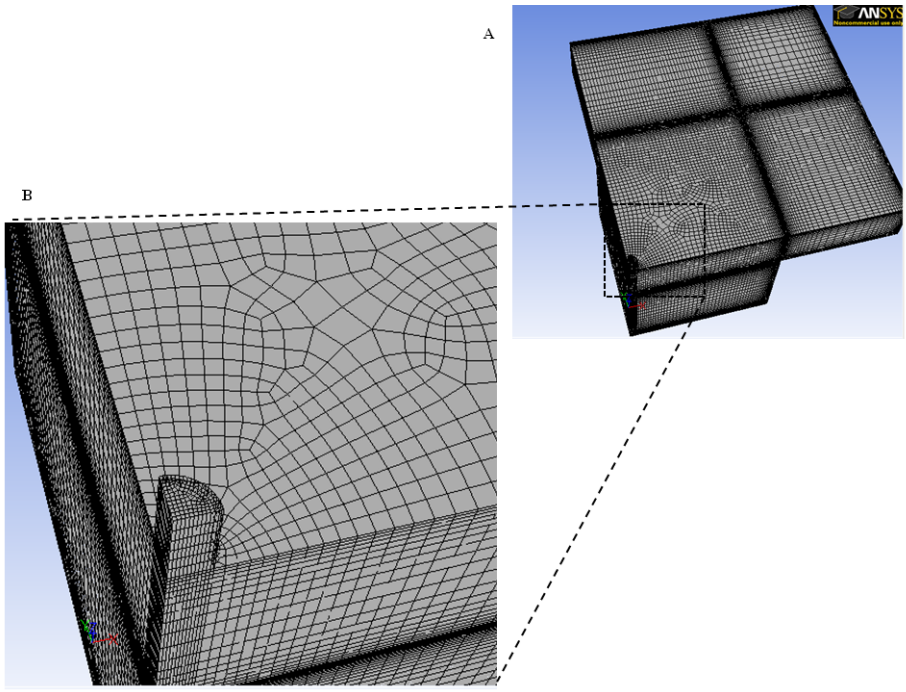

Figure 2.3.4a: Cubic configuration (A) hexahedral mesh of quarter section of cubic scaffold-cavity assembly with boundary details (B) mesh around the tip of the needle

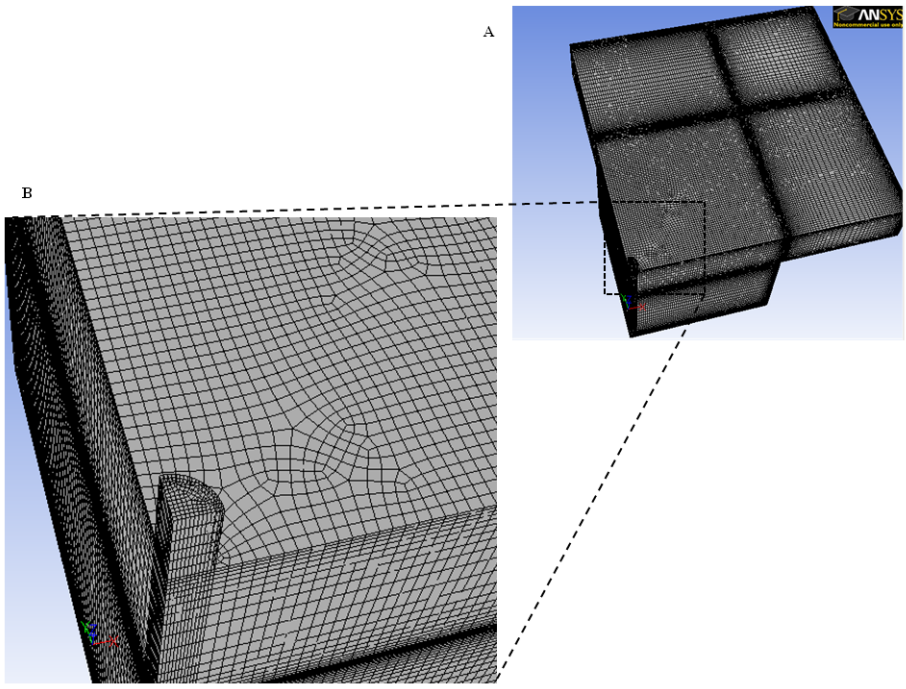

Figure 2.3.4b: Refined cubic configuration (A) Refined hexahedral mesh of quarter section of cubic scaffold-cavity assembly with boundary details (B) mesh around the tip of the needle

2.4 Model Assumptions and Boundary Conditions

Furthermore, it is important to note that modeling the scaffold pores and the interconnecting channels between pores is beyond the scope of this paper. Detailed simulation of the individual pores would make the model a two-scale problem that would require multi-million-mesh models and possibly create high levels of numerical round off errors. Hence, it is impossible to obtain an exact match between experimental and numerical modeling.

2.4.1 Scaffold Modeling

Since the pores and interconnecting channels are not modeled in details, the flow through the scaffold was simulated as flow through a porous media that obeys the Darcy's law. Therefore, the porous media model in ANSYS FLUENT was used to model the flow through the scaffold. In this model, the Darcy law:

$$\Delta p = -\frac{\mu}{\alpha}\vec{v}$$

was solved in the porous region. The volume blockages that was physically present was not represented. Therefore, the superficial velocity inside the porous region based on the volumetric flow rate was reported in other to ensure the continuity of the velocity vector across the porous region interface.

2.4.1 Fluid Phase Modeling

The liquid phase, Mesenpro RS media (Gibco, Invitrogen Corporation Carlsbad, CA), was represented as an incompressible, homogeneous, Newtonian fluid with density and viscosity of 1000 kg/m^3 and 1.45 x 10^{-3} Pa-s respectively. CFD transient volume of fluid (VOF) formulation with the parameters are: 3-D, laminar fluid flow, pressure inlet boundary condition (atmospheric

pressure) and no slip boundary conditions on walls was used to simulate the mixture in the cavity (figure 2.4.1). The VOF formulation in ANSYS FLUENT is able to model two or more immiscible fluids with clearly defined interface. In each control volume, all phases share a single set of momentum equations and the sum of the volume fraction of all phases is unity. The volume fraction of the phases are determined in each computational cell and tracked throughout the domain. To obtain this volume fraction in a two-phase model, for each computational cell, the continuity equation shown below was solved for the secondary phase (media):

$$\frac{1}{\rho_s}\left[\frac{\partial}{\partial t}(\alpha_s\rho_s) + \nabla.\,(\alpha_s\rho_s\vec{v}_s) = S_{\alpha_s} + \sum_{p=1}^{n}(\dot{m}_{ps} - \dot{m}_{sp})\right] \qquad (2.1)$$

Note that in this study there is no mass transfer between the two phases therefore $\dot{m}_{sp}$ and $\dot{m}_{ps}$ are zero.

The following constraint is used to obtain the volume fraction of the primary phase:

$$\alpha_s + \alpha_p = 1 \qquad (2.2)$$

A standard finite-difference interpolation scheme (explicit approach) was used to discretize equation (2.1):

$$\frac{\alpha_s^{n+1}\rho_s^{n+1} - \alpha_s^n\rho_s^n}{\Delta t}V + \sum_f(\rho_s U_f^n \alpha_{s,f}^n) = \left[\sum_{p=1}^{n}(\dot{m}_{ps} - \dot{m}_{sp}) + S_{\alpha_s}\right]V \qquad (2.3)$$

Similarly, the momentum equation

$$\frac{\partial}{\partial t}(\rho\vec{v}) + \nabla.(\rho\vec{v}\vec{v}) = -\nabla p + \nabla.[\mu\,(\nabla\vec{v} + \nabla\vec{v}^{\mathrm{T}})] + \rho\vec{g} + \vec{F} \qquad (2.4)$$

was solved in each computational cell in other to determine the shared velocity field. The SIMPLE (Semi-Implicit Method for Pressure Linked Equation) algorithm was used to solve equation (2.4). This algorithm enables full pressure-velocity coupling during the solution of the equation. In the method, equation (2.4) was first discretized as shown below:

$$a_p\left(\boldsymbol{u}^{(m)}\right)u^*_{i,p} + \sum_l a_{l,p}\left(\boldsymbol{u}^{(m)}\right)u^*_{i,l} = Q_p\left(\boldsymbol{u}^{(m)}\right) - \left(\frac{\delta p^{(m)}}{\delta x_i}\right)_p \qquad (2.5)$$

And the solution of equation (2.5), u_i^*, was obtained with $p^{(m)}$ used as an estimate pressure. Note that u_i^* does not satisfy the incompressibility condition. Thus, the continuity equation together with the value of u_i^* was used to obtain pressure correction p'. Following this, the new values of velocity and pressure were determined as

$$u_i^{(m+1)} = u_i^* + u_i', \quad p^{(m+1)} = p^{(m)} + p' \qquad (2.6)$$

Note: 20 iterations were performed for every time step.

At the beginning of the simulation, the domain representing scaffold- cavity assembly was patched with a gauge pressure of -100kPa as recommended by Govil et al. (US Patent 2010/0155282 A1) and volume fraction of liquid phase equal 1 was patched to the tip of the needle (figure 2.4.2). After approximately 0.25 milliliters (ml) of the cell suspension has been injected into the cavity, the volume fraction of the liquid phase was set to zero to stop the injection. Air was initially modeled with the ideal gas law but at the end of the injection the density of air was changed to a constant (1.225 kg/m^3).The variable time-stepping was used in the simulation for a total of 2 seconds. The transient results were written at different time points and post-processed by quantifying the velocity and pressure profiles on different sections of the

scaffold as well as the volume fraction of the liquid phase and the wall shear stresses. The CFD simulations were performed on a 64-Bit Linux computer cluster using 4 CPUs in parallel.

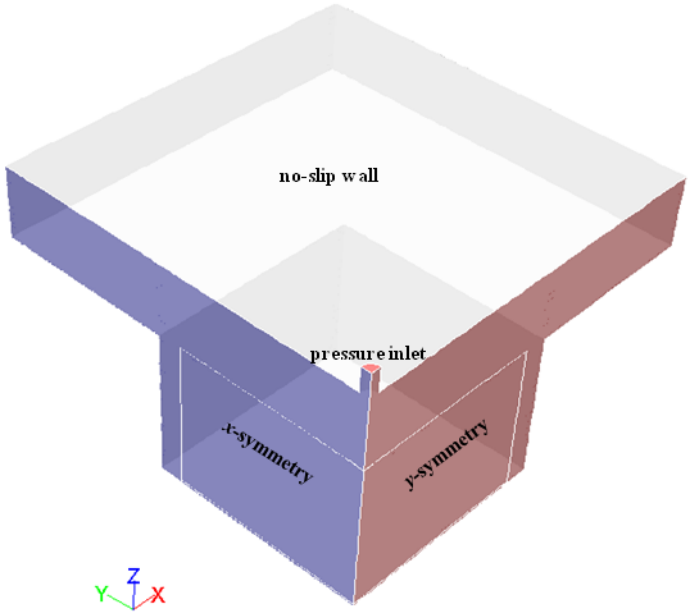

Figure 2.4.1: Cubic scaffold-cavity assembly boundary conditions

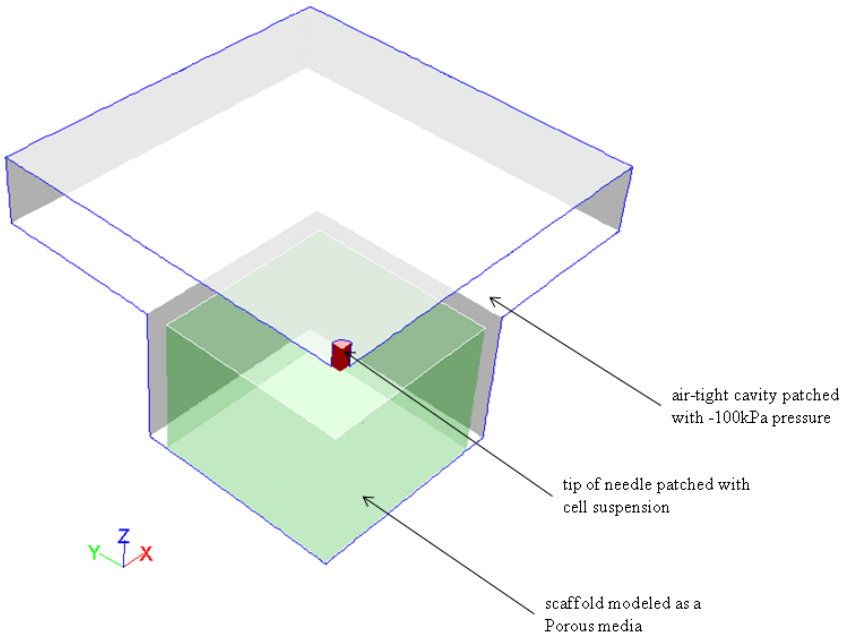

Figure 2.4.2: Cubic scaffold-cavity assembly initial conditions

2.4.2 Cell Presence Modeling

ANSYS FLUENT discrete phase model (DPM) was used to mimic the presence of the cells. In the model, the trajectory of the discrete phase particles was obtained by integrating the force balance on the particle in a Lagrangian frame of reference. The force balance was written as

$$m_p \frac{\partial \boldsymbol{u}_p}{\partial t} = \boldsymbol{F}_{drag} + \boldsymbol{F}_{pressure} + \boldsymbol{F}_{virtual\ mass} + \boldsymbol{F}_{gravity} + \boldsymbol{F}_{other} \qquad (2.7)$$

$$\boldsymbol{F}_{drag} = \frac{3}{4} m_p \frac{\rho}{\rho_p} \frac{C_D}{d_p} \|\boldsymbol{u} - \boldsymbol{u}_p\| \qquad (2.7a)$$

$$\boldsymbol{F}_{pressure} = -\frac{m_p}{\rho_p} \nabla p \qquad (2.7b)$$

$$\boldsymbol{F}_{virtual\ mass} = \frac{m_p}{2} \frac{\rho}{\rho_p} \frac{d(\boldsymbol{u} - \boldsymbol{u}_p)}{dt} \qquad (2.7c)$$

$$\boldsymbol{F}_{gravity} = m_p \frac{\rho_p - \rho}{\rho_p} \boldsymbol{g} \qquad (2.7d)$$

The cells were modeled as spherical particles with 6 µm diameter and dispersed in the continuous liquid phase. A One-Way coupling approach was employed in the simulation. That is, the effect of the discrete phase on the continuous phase is neglected and the discrete phase pattern is predicted based on the continuous phase flow field. A number of 0.25 x 10^{-6} ELA cells were injected through the inlet with a uniform surface distribution.

2.5 Determining Optimal Cell Seeding Pressure

To determine the optimal vacuum pressure for cell seeding, two simulations were performed in addition to the simulation described above. To achieve this goal, the first step was to patch the domain representing the scaffold- cavity construct with a gauge pressure of -60 kPa at the beginning of the simulation (case 1) then in a similar approach patch the domain representing the scaffold- cavity construct with a gauge pressure of -20 kPa at the beginning of the second simulation (case 2). In both cases, all other conditions were similar to conditions described in section 2.4.1 and 2.4.2 above.

2.6 Modeling Flow in a Cylindrical Configuration Using Determined Optimal Initial Vacuum Pressure

In a new simulation, the optimal vacuum pressure obtained in section 2.5 was used to simulate the flow of the cell suspension in a seeding device with a cylindrical cavity and scaffold. Similarly, a laminar transient CFD volume of fluid (VOF) formulation was used t model the flow The new case comprises of; a pressure inlet boundary condition (atmospheric pressure), no slip boundary conditions on walls and symmetry conditions at the cross-section. At the beginning of the solution, the domain representing the cavity was patched with -20 kPa gauge pressure and the domain representing the tip of the needle was patched with the cell suspension. The solution was allowed to proceed for a total of two seconds and 0.25 ml of the cell suspension (containing 250, 000 ELA cells) was injected into the cavity.

RESULTS

3.1 Investigating Symmetry

To investigate whether a quarter section of the cubic scaffold- cavity assembly can successfully model the fluid flow in the full geometry, CFD cases were simulated for the full geometry and quarter section of the geometry. Since the objective was to determine the presence of symmetry, grid independent solution was not obtained for both cases. However, to limit bias that may be introduces as a result of computational errors, both geometries were meshed with proportional number of hexahedrons. That is, the full and the quarter geometry contain 487,192 and 121,798 hexahedrons respectively. The modeling assumptions was kept the same for both cases but the boundary conditions for the quarter model are pressure inlet, symmetry (*x*-*z* plane) and symmetry (*y*-*z* plane) and a no slip wall. The full model contains a pressure inlet and no-slip wall. The simulations for both cases were run for approximately 0.001 seconds after which the results were inspected for similarities (figure 3.1.1 A-D). The plots of the static pressure of the mixture (air and media) along the centerlines in the z-direction (a line through the center of the *x*-*y* plane) and the y-direction (line through the center of the x-z plane) for both the quarter and the full model revealed similar profiles (figure 3.1.1 A and B). Similarly, the plots of the velocity magnitude of the mixture (air and media) along the centerlines in the z-direction (a line through the center of the *x*-*y* plane) and the y-direction (line through the center of the *x*-*z* plane) for both the quarter and the full model revealed close correlation between both plots (figure 3.1.1 C and D).

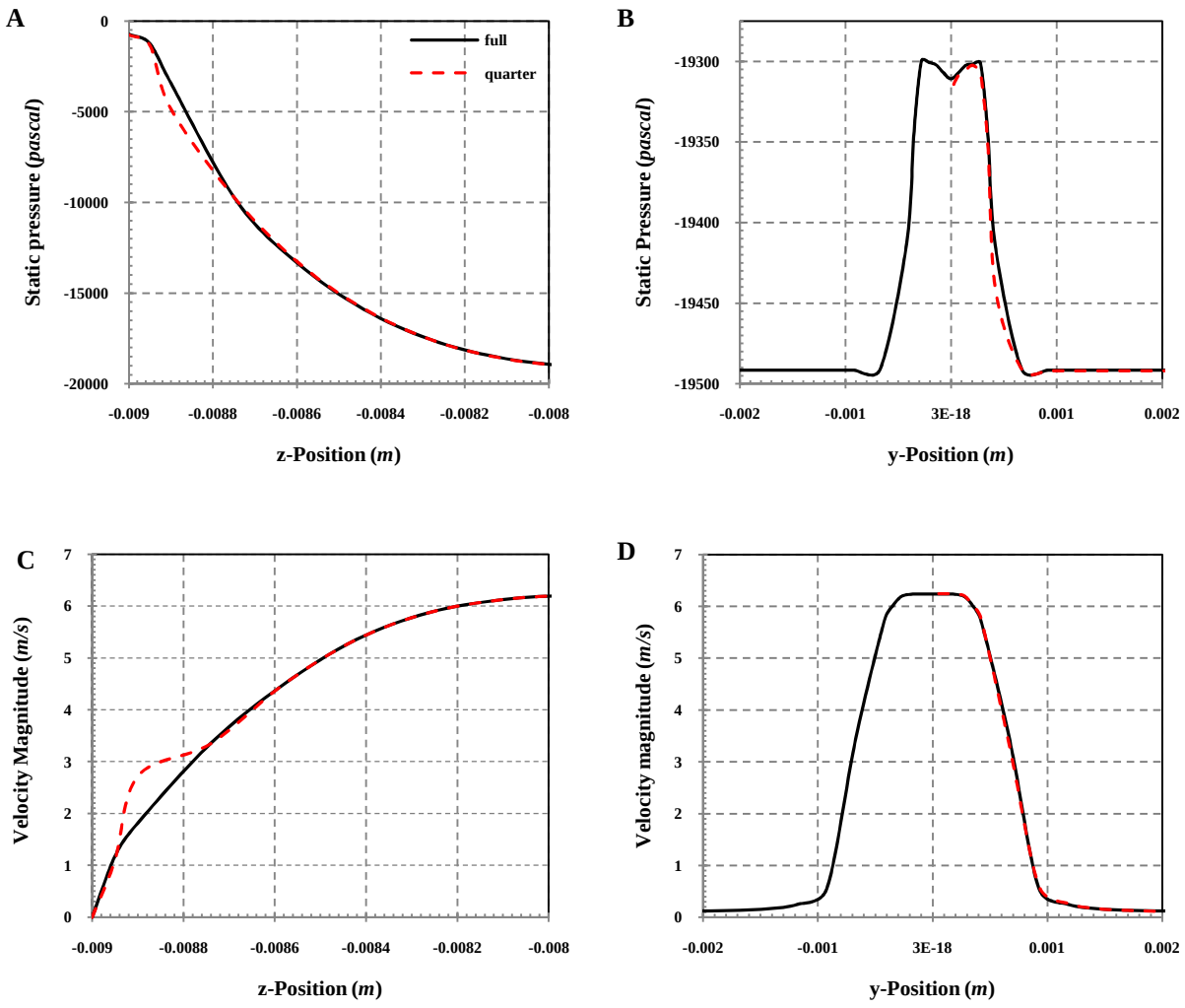

Figure 3.1.1: Investigate symmetry in the cubic scaffold- cavity assembly. (A) Variation of static pressure for the mixture along the centerline in the z-direction for both the full model and the quarter model. (B) Variation of static pressure for the mixture along the centerline in the y-direction for both the full and the quarter model. (C) Variation of the velocity magnitude of the mixture along the centerline in the z-direction for both the full and the quarter model. (D) Variation of velocity magnitude of the mixture along the centerline in the y-direction for both the full and the quarter.

3.2 Transient Profile in Cubic Scaffold-Cavity Assembly Using -100kPa Gauge Pressure

An important benefit of computational fluid dynamics methods is that it allows detailed visualization of parameters associated with fluid flow e.g. velocity, pressure, shear stresses, volume fraction of phases etc. Therefore, the distribution of the volume fraction of the cell suspension (figure 3.2.1), velocity of the mixture (figure 3.2.2) and the hydrostatic pressure (figure 3.2.3) were plotted and analyzed at different time points. For the volume fraction of the cell suspension, values between 0.5 and 1 were displayed at six different time points (figure 3.2.1). Results from the CFD solution revealed that it took 0.14 seconds for approximately 0.25ml of the cell suspension to be injected into the air-tight cavity. This value was not far from the 0.2 seconds that was obtained in an initial preliminary study. As shown in figure 3.2.1, most of the scaffold volume was not soaked with the cell suspension. At t = 2 seconds, only 44% of the volume of the cell suspension was in the scaffold. A very low gauge pressure (-100 kPa) in the air-tight cavity compared to the atmospheric pressure at the inlet resulted in a high differential pressure, producing a high initial mass flow rate (1.86 e-03 kg/s at t = 1.0 e-03). Thus, the cell suspension travelled up the side walls of the air-tight cavity unto the top walls of the cavity and spilt into the upper chamber of the air-tight cavity. Figure 3.2.2 shows the distribution of the velocity magnitude on nine different cross-sections of the scaffold at 4 different time points. The nine cross-sections include:

- three cross-sections perpendicular to the x-axis at x = 0, 4 and 8mm.
- three cross-sections perpendicular to the y-axis at y = 0, 4 and 8mm
- three cross-sections perpendicular to the z-axis at z = -2.9, -5.9 and -8.9mm

Since perfusion of the scaffold is of more importance in this study, these cross-sections were selected to correspond to regions in the scaffold and the time points spanned the time shortly after the injection of the cell suspension was completed and the cell suspension almost stopped moving in the cavity. As expected, for all of the cross-sections, the velocity magnitude was higher in regions of lower pressure (figure 3.2.2 and figure 3.2.4). At time point t = 0.16 seconds, regions of higher flow velocities were observed on the cross-sections x = 8mm and x = 4mm of the scaffold parallel to the y-axis (figure 3.2.3). These regions have higher velocity in the z-direction than in the x- and y- directions (Table 3.2.1). For cross-sections parallel to the x-axis, regions of higher velocity magnitude were notices on the section x = 4mm (figure 3.2.3). This region has higher velocity in the negative x-direction than in the y- and z-direction (Table 3.2.2) For cross-sections parallel to the x-y-axis, regions of higher velocity magnitudes were observed on the section z =-2.9 and -5.9mm. These sections have higher velocity in the positive z-direction compared to the x- and y-directions (Table 3.2.3). At a later time, t = 0.18 seconds, higher flow velocity was observed in the region of the scaffold nearer to the center of the scaffold and region of the scaffold nearer to the top wall (x = 4, y= 4 and z = -0.29mm).When compared to results in Table 3.2 the highest fluid flow velocity (0.9294 *m/s*) was observed in the positive z-direction (Table 3.2.2). This is in agreement with the gradual pressure build up in the cavity. In contrast to the earlier time point, fluid velocities in both the positive x- and y-direction are higher than in the corresponding negative directions and much lower when compared to the earlier time point. This revealed a much lower flow of fluid out of the upper region of the scaffold. In comparison to the corresponding plot of volume fraction at the time point, the fluid flowing out is identified as air and not the cell suspension. The remaining time points shown in figure 3.2.2 depicts a gradual

reduction in the flow velocity distribution from the region of the scaffold nearer to the cavity side and top walls to the center of the scaffold.

As it could be anticipated, there was an initial sudden build up of pressure in the cavity, -100 kPa to 75 Pa in 0.16 seconds, (table 3.2.2) followed by a gradual build up in the static pressure. Shortly after injection of the cell suspension was completed, t = 0.16 seconds, the maximum and minimum static pressure obtained at the center of the scaffold (cross section parallel to the x- and y- axis and at y = 0 and x = 0 mm respectively) and the surface of the scaffold (cross section parallel to the x- and y- axis and at y = 8 and x = 8 mm respectively) were 75.15 Pa and -27.15 Pa respectively (table 3.2.2). The center of the scaffold showed a higher pressure build up compared to the surface of the scaffold. This agrees with lower velocities that were observed in the center part of the scaffold in the velocity magnitude contour plot (figure 3.2.2). Later time points showed a gradual reduction in the maximum and an increase in the minimum pressure. In addition, figure 3.2.3 depicts this gradual increase along the positive z-direction. In general, the buildup of the static pressure at the surface of the scaffold occurred at a slower rate compared to the center. A large number of the cells were observed on the upper chamber of the cavity. This indicated an ineffective seeding of the scaffold (figure 3.2.5).

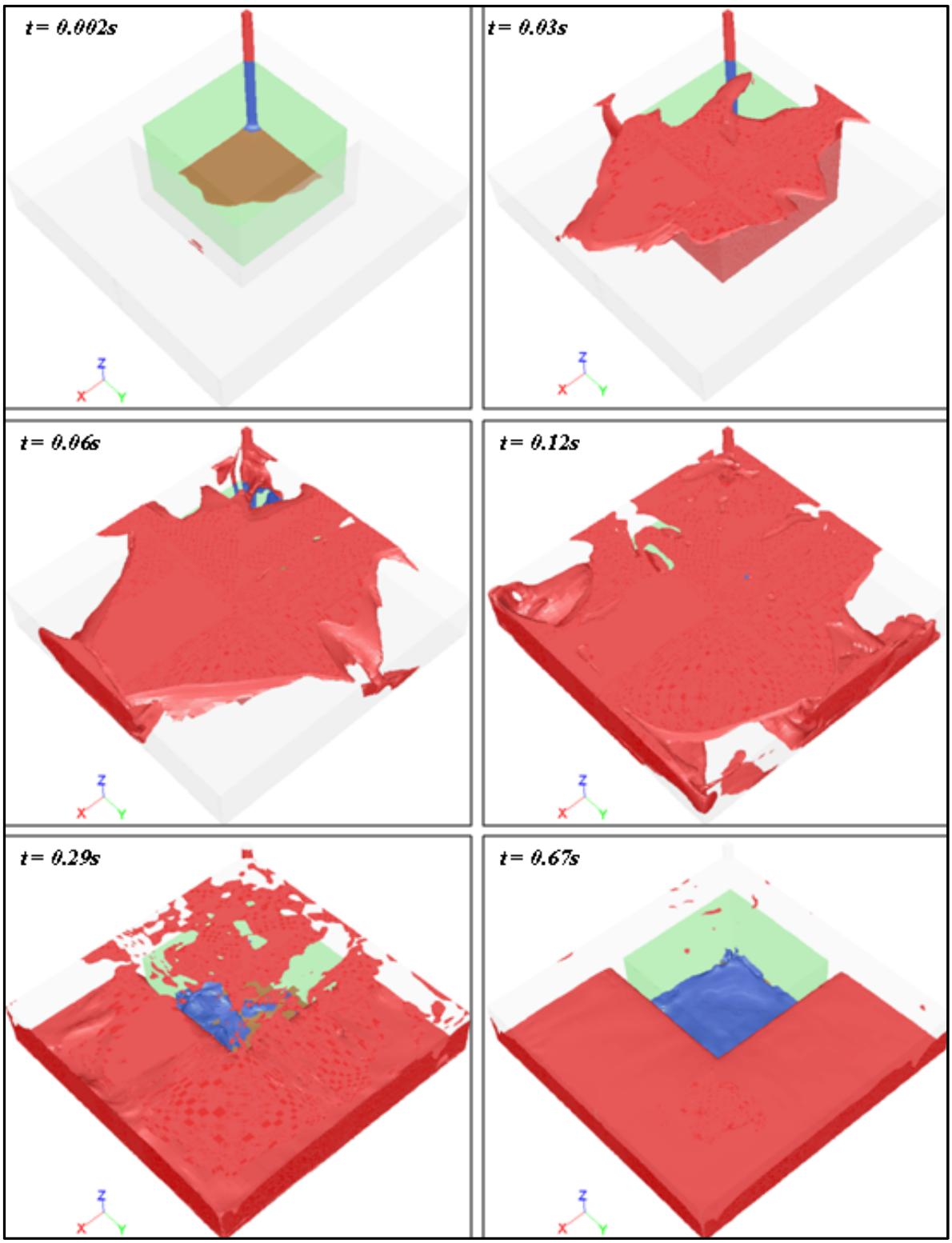

Figure 3.2.1: Liquid phase volume fraction (0.5 -1.0) distribution in the scaffold- cavity assembly after 0.67 seconds for -100kPa initial vacuum pressure. Blue color indicates the fraction of the liquid phase that is in the scaffold and the red color indicates the fraction of the liquid that is not in the scaffold.

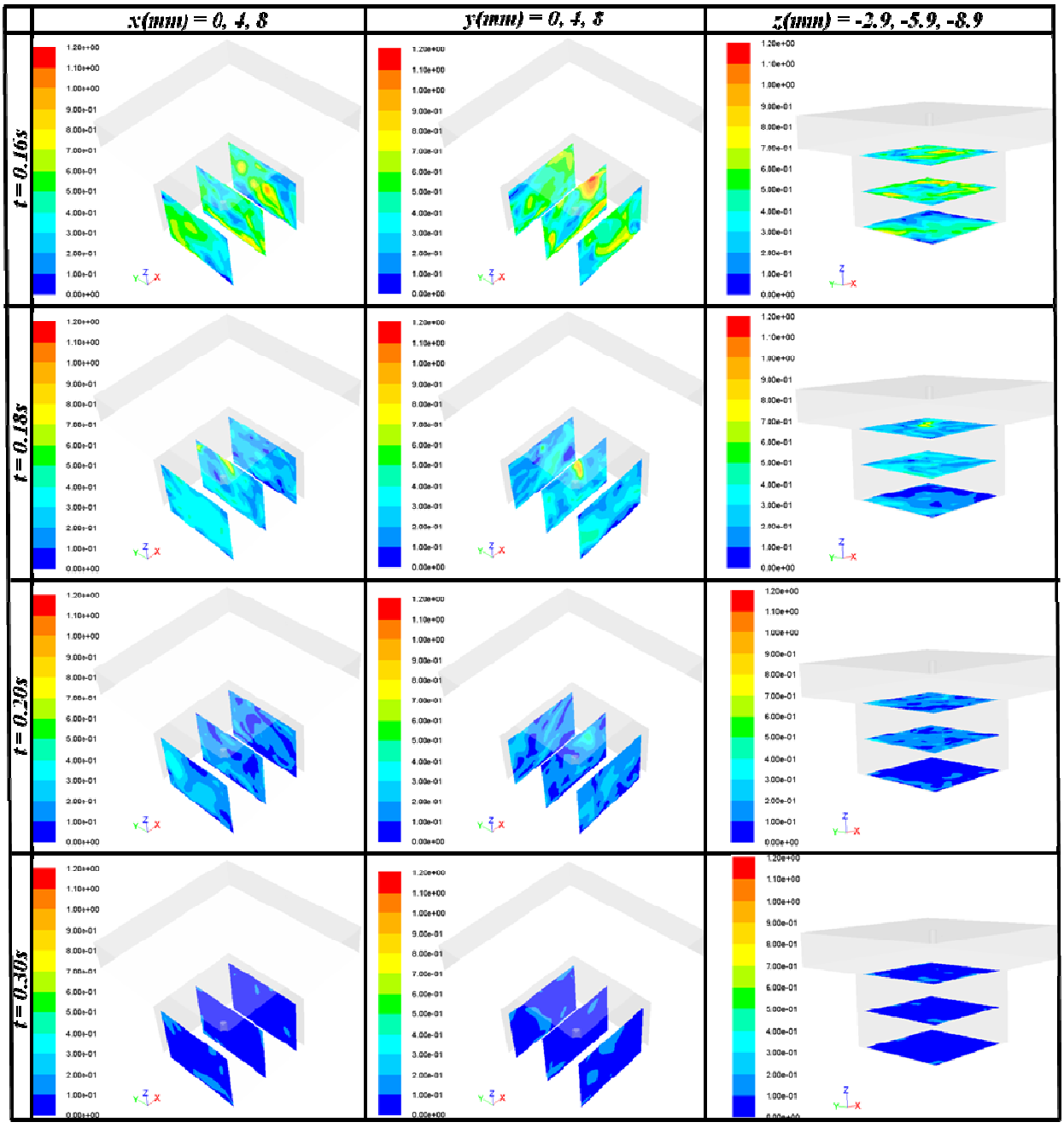

Figure 3.2.2: Velocity magnitude distribution for -100 kPa initial vacuum pressure. The velocity field on cross-sections perpendicular to the *x*-plane (*x* = 0mm, 4mm, 8mm), *y*-plane (*y* = 0mm, 4mm, 8mm) and *z*-plane (*z* = -2.9mm, -5.9mm, -8.9mm) at time *t* = 0.16s, 0.18s, 0.20s and 0.30s.

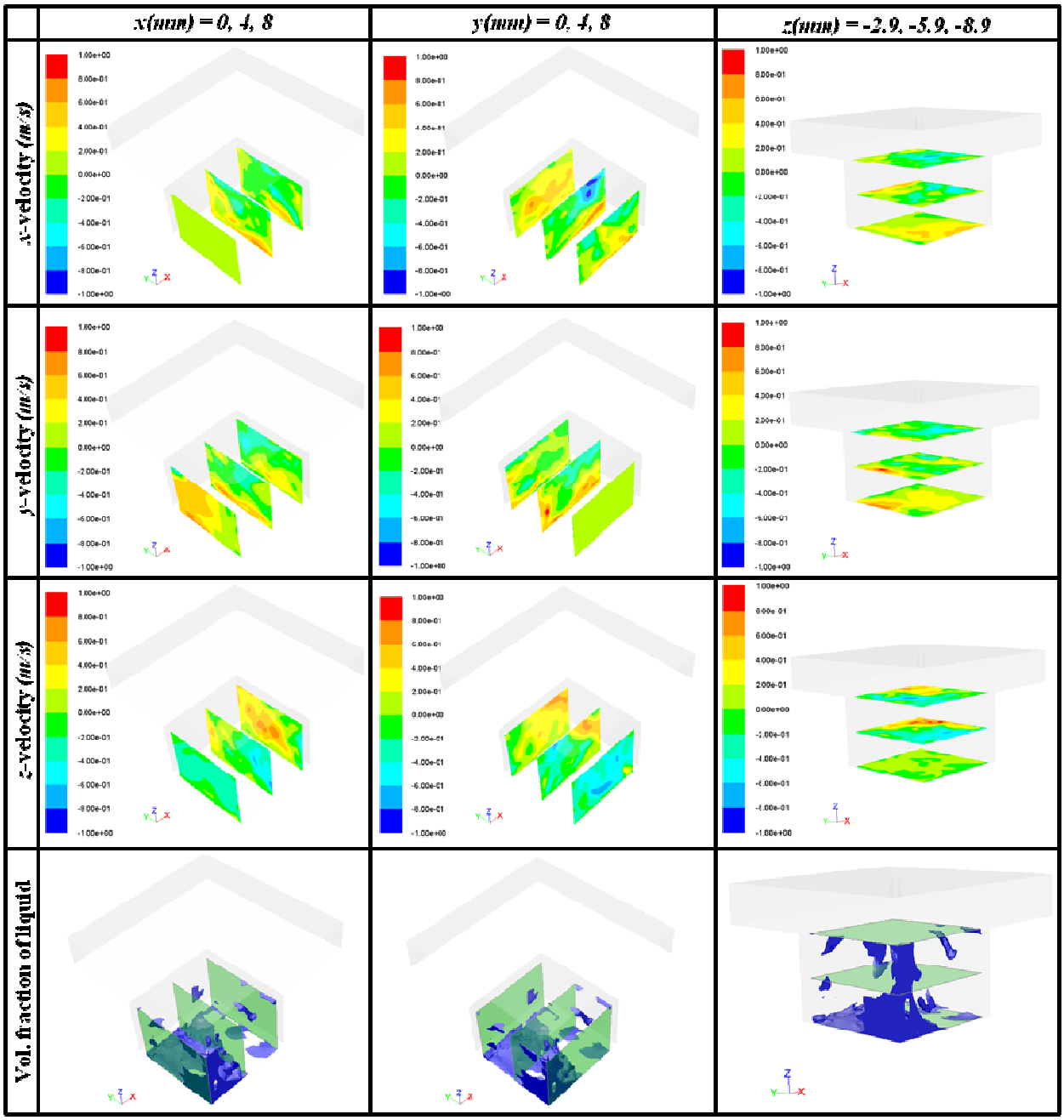

Figure 3.2.3: Contour of the components of velocity of mixture and volume fraction of the cell suspension (0.5 - 1) for -100 kPa initial vacuum pressure at time t = 0.16 seconds. The components of the velocity field on cross-sections perpendicular to the x-plane (x = 0mm, 4mm, 8mm), y-plane (y = 0mm, 4mm, 8mm) and z-plane (z = -2.9mm, -5.9mm, -8.9mm) and the corresponding volume fraction contour at time t = 0.16s.

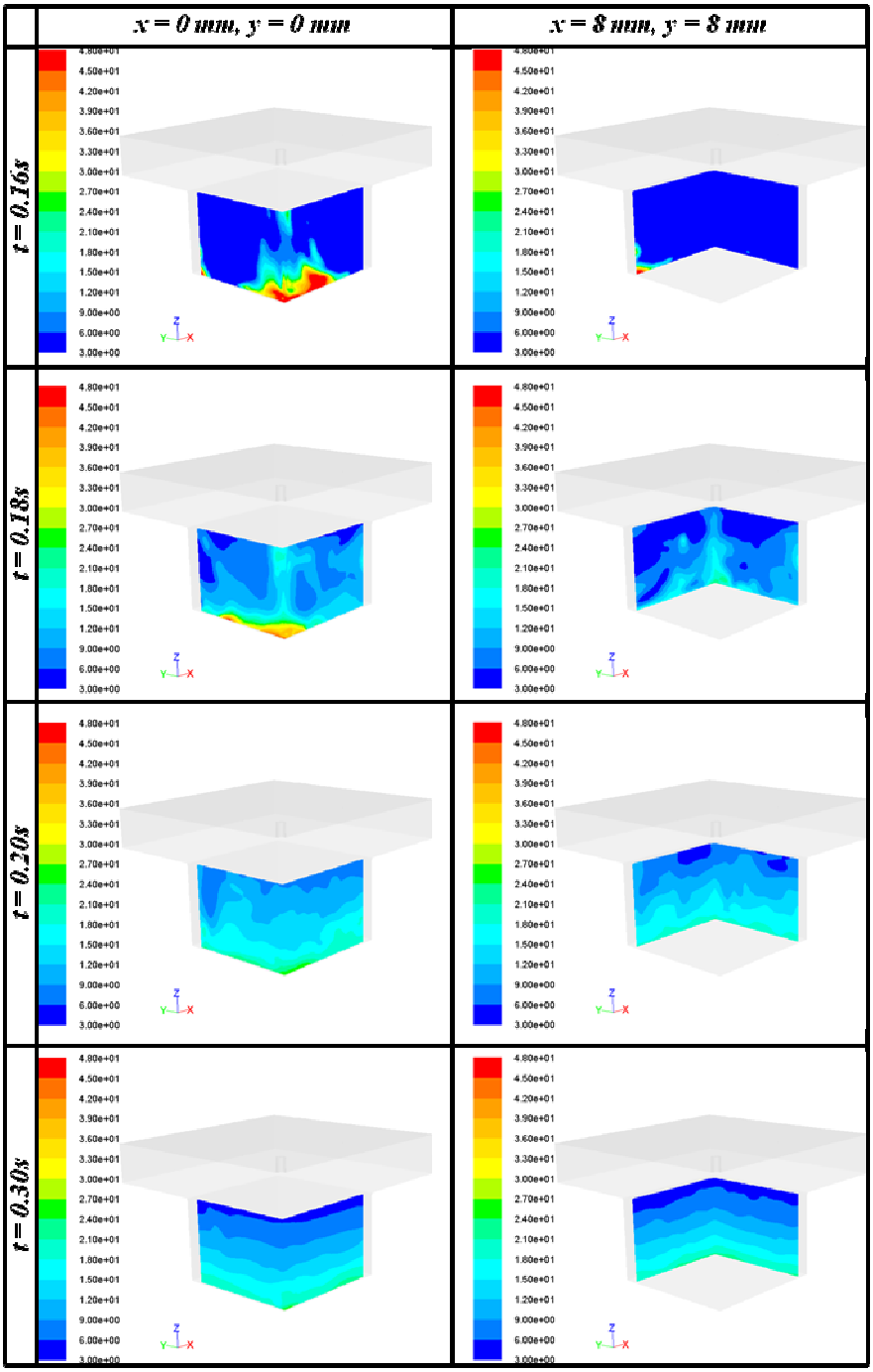

Figure 3.2.4: Static pressure distribution for -100kPa initial gauge pressure. The static pressure contour on cross section parallel to the *x*-axis (*y* = 0mm, *y*= 8mm) and *y*- axis (*x* = 0mm, *x* = 8mm)

Table 3.2.1: Summary of for initial vacuum pressure = -100kPa on cross-sections parallel to the *y*-axis.

		Static pressure	**Velocity magnitude**	***x*-velocity**	***y*-velocity**	***z*-velocity**
		(*pa*)	**(*m/s*)**	**(*m/s*)**	**(*m/s*)**	**(*m/s*)**
t* = 0.16*s	max	63.57	1.0059	0.6945	0.7410	0.7992
	min	-23.44	0.0126	-0.5709	-0.5210	-0.7084
t* = 0.18*s	max	47.10	0.8230	0.4052	0.3506	0.7072
	min	-3.16	0.0114	-0.5497	-0.4734	-0.3782
t* = 0.21*s	max	27.26	0.3985	0.2837	0.3953	0.2088
	min	3.38	5.71 e-03	-0.2339	-0.2394	-0.2525
t* = 0.29*s	max	25.97	0.2052	0.0811	0.1618	0.1662
	min	4.06	2.58 e-03	-0.0988	-0.1399	-0.1300

Table 3.2.2. Summary of results for initial vacuum pressure = -100 kPa on cross-sections parallel to the *x*-axis.

		Static pressure	**Velocity magnitude**	***x*-velocity**	***y*-velocity**	***z*-velocity**
		(*pa*)	**(*m/s*)**	**(*m/s*)**	**(*m/s*)**	**(*m/s*)**
t* = 0.16*s	max	75.16	1.2130	0.8054	0.8909	0.7103
	min	-27.15	0.0126	-0.9633	-0.4620	-0.7118
t* = 0.18*s	max	47.10	0.9535	0.4071	0.3423	0.9294
	min	2.03	9.67 e-03	-0.5076	-0.3360	-0.4057
t* = 0.21*s	max	26.31	0.4699	0.2852	0.2921	0.3881
	min	4.32	5.71 e-03	-0.2945	-0.2117	-0.2599
t* = 0.29*s	max	25.96	0.1846	0.1025	0.1346	0.1841
	min	3.8756	2.58 e-03	-0.0100	-0.1219	-0.1577

Table 3.2.3. Summary of results for initial vacuum pressure = -100 kPa on cross-sections parallel to the x-y plane.

		Static pressure	**Velocity magnitude**	***x*-velocity**	***y*-velocity**	***z*-velocity**
		(*pa*)	**(*m/s*)**	**(*m/s*)**	**(*m/s*)**	**(*m/s*)**
t* = 0.16*s	max	75.16	1.0231	0.6291	0.8667	0.8942
	min	-24.18	0.0127	-0.7864	-0.6404	-0.6759
t* = 0.18*s	max	51.85	0.8000	0.3477	0.3514	0.7265
	min	1.77	9.0 e-03	-0.3885	-0.3147	-0.4116
t* = 0.21*s	max	27.27	0.4595	0.2657	0.3940	0.3459
	min	4.31	5.18 e-03	-0.2630	-0.1653	-0.2490
t* = 0.29*s	max	25.98	0.1846	0.1000	0.1479	0.1841
	min	3.84	1.97 e-03	-0.0873	-0.1175	-0.1441

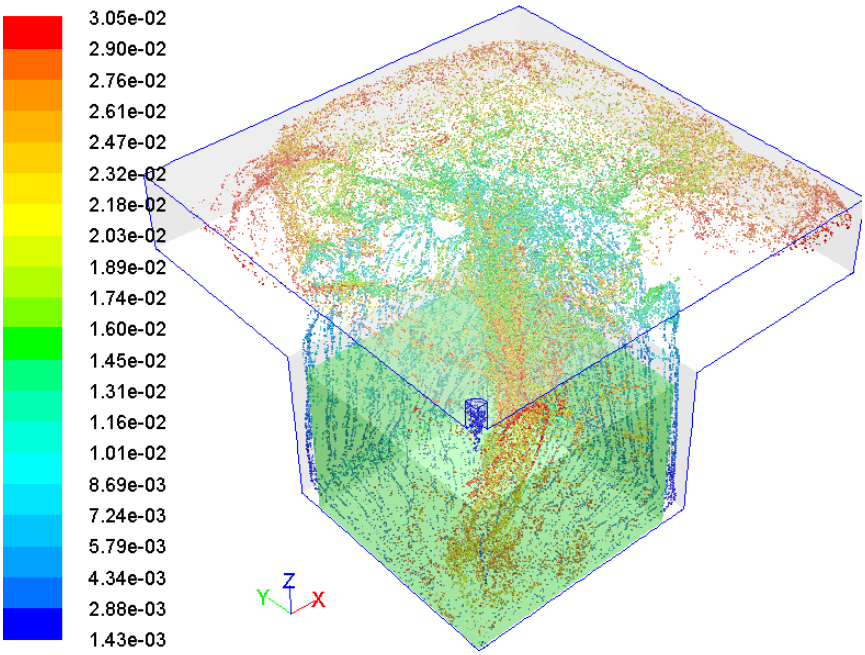

Figure 3.2.5: Distribution of the cells in the scaffold and cavity at *t* = 0.14 seconds for -100kPa initial vacuum pressure. The cells are colored by the residence time in seconds.

3.3 Effect of decreasing the Initial Vacuum Pressure on Fluid Flow

In an attempt to limit the flow of the cell suspension up the side walls and unto the top walls of the cavity, another case (with identical boundary conditions and mesh) was simulated for the scaffold-cavity assembly. However, in this new case the domain representing the cavity was patched with -60 kPa gauge pressure at the beginning of the solution. The rationale for the decreased vacuum pressure was to reduce the resulting pressure differential and thus reduce the initial flow velocity on the walls of the cavity in order to prevent the cell suspension from spilling over into the upper section of the cavity. The simulation took 0.18 seconds to inject 0.25ml of the cell suspension into the cavity. Though the initial mass flow rate at the inlet was lesser (1.43 e-03 *kg/s* at t = 1.0 e-03 seconds), it was not enough to prevent the cell suspension from spilling into the upper section of the cavity (figure 3.3.1). It was observed that only 48% of volume of the cell suspension soaked the scaffold at t = 2 seconds. Similarly, figure 3.3.2 shows the distribution of the velocity magnitude on cross sections of the scaffold as described earlier and at four different time points. At time t = 0.20 seconds, the cross-sections parallel to the y-axis have more pockets of higher velocity magnitude on the lower region of the section at x = 4mm and the middle of x = 0mm than any other region of the sections. Though the velocity in the positive z-direction appeared to be the highest (table 3.3.1) for these sections, when these regions with higher velocities were compared with figure 3.3.3, it was observed that the velocity in the positive y- and z-direction was greater than in the x- direction for the cross-section x = 4mm and 0mm.This indicated a flow in the positive y and z-direction. The cross-sections parallel to the x-axis have more pockets of higher velocities on the top right region of the section at y = 0mm, lower region of section y = 4mm and lower region of section y = 0mm than in any other region.

Comparing these regions of higher velocities to identical regions in figure 3.3.3 the following were observed higher velocities in the negative x-direction and in the positive y-direction (table 3.3.2). Taken together, this indicated that air is been forced up near the surface of the scaffold while the cell suspension is flowing towards the center of the scaffold. Also, for the cross-sections parallel to the *x*-*y* axis more pockets of higher velocity magnitude were observed on the centers and corners (near the side walls) of section *z* = -5.9mm and *z* = -2.9mm than in any other region. For the two sections with regions of higher velocity magnitude, the high velocities were in the positive *z*- and *y*-direction near the vertical surfaces and the lower horizontal surface of the scaffold respectively (figure 3.3.3 and table 3.3.3) which was consistent with air being forced up near the surface of the scaffold as observed in other sections. In general, later time points revealed gradual decrease in the velocity magnitude on the different cross-sections, with higher velocities in regions mostly closer to the center of the scaffold (for sections parallel to the *x*- and *y*-axis) and top of the scaffold (for sections parallel to the z-axis).Similar to the static pressure profile for the earlier case, there was an initial sudden build up of pressure in the cavity, -60 kPa to 140.40 Pa in 0.20 seconds. This was followed by a gradual pressure build up with higher rates in the middle of the scaffold than on the outer surfaces of the scaffold nearer to the side walls. In addition, the pressure build up was predominantly along the positive *z*-direction. At t = 0.37 seconds, the rate of pressure build up on the surface of the scaffold (near side walls) was almost identical to the pressure build up at the center of the scaffold (figure 3.3.4). Table 3.2 reports the summary of the static pressure, velocity magnitude, *x*-velocity, y-velocity, *z*-velocity on all the sections combined and shear stresses on the walls of the cavity. Figure 3.3.5 reports the distribution of the cells on the scaffold and the cavity. Similar to figure 3.2.5, an inefficient seeding was observed.

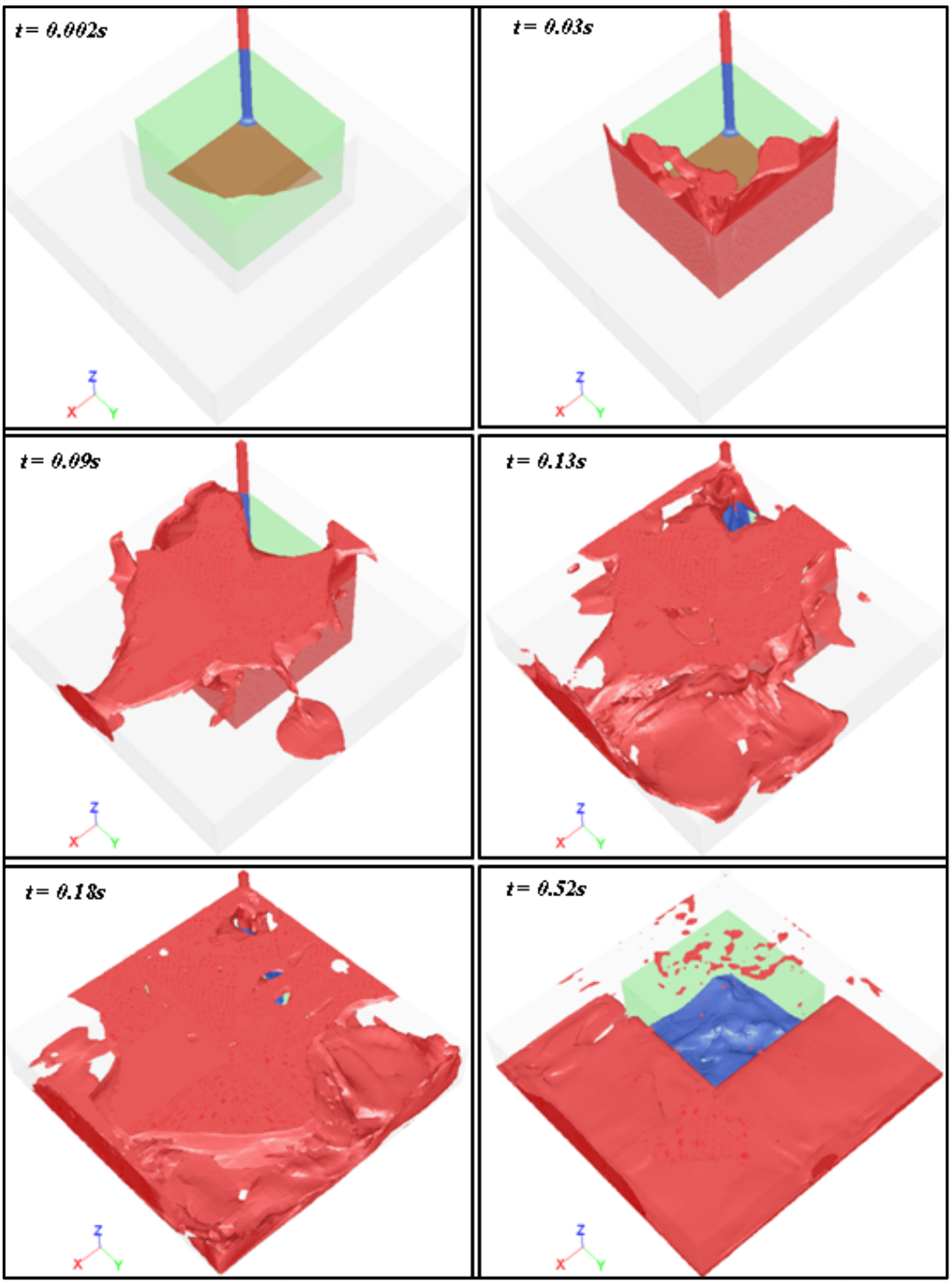

Figure 3.3.1: Liquid phase volume fraction (0.5 -1.0) distribution in the scaffold- cavity assembly after 0.52 seconds for -60 kPa initial vacuum pressure. Blue color indicates the fraction of the liquid phase that is in the scaffold and the red color indicates the fraction of the liquid that is not in the scaffold.

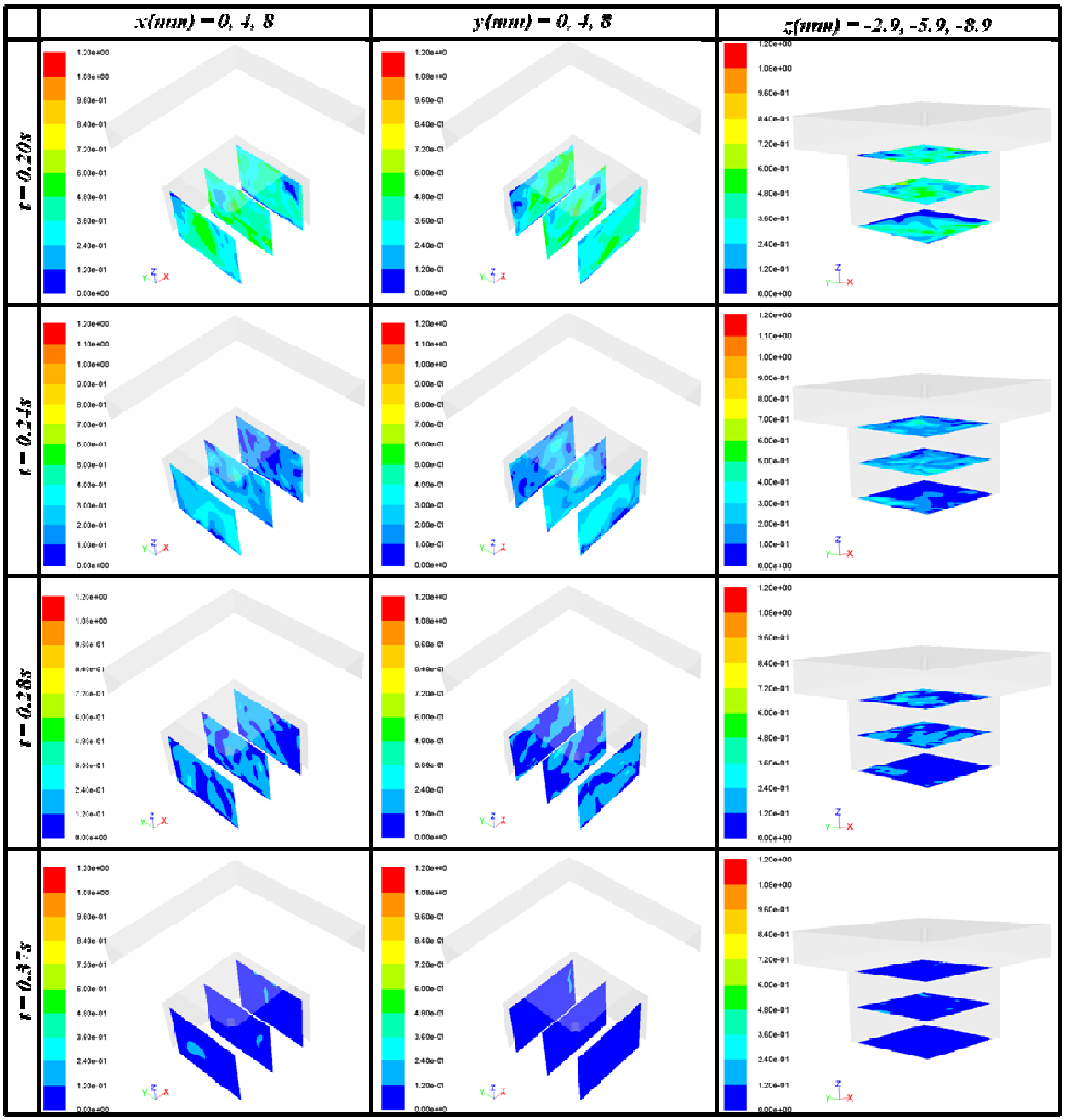

Figure 3.3.2: Velocity magnitude distribution for -60 kPa initial vacuum pressure. The velocity field on cross-sections perpendicular to the *x*-plane (*x* = 0mm, 4mm, 8mm), *y*-plane (*y* = 0mm, 4mm, 8mm) and *z*-plane (*z* = -2.9mm, -5.9mm, -8.9mm) at time *t* = 0.20s, 0.24s, 0.28s and 0.37s.

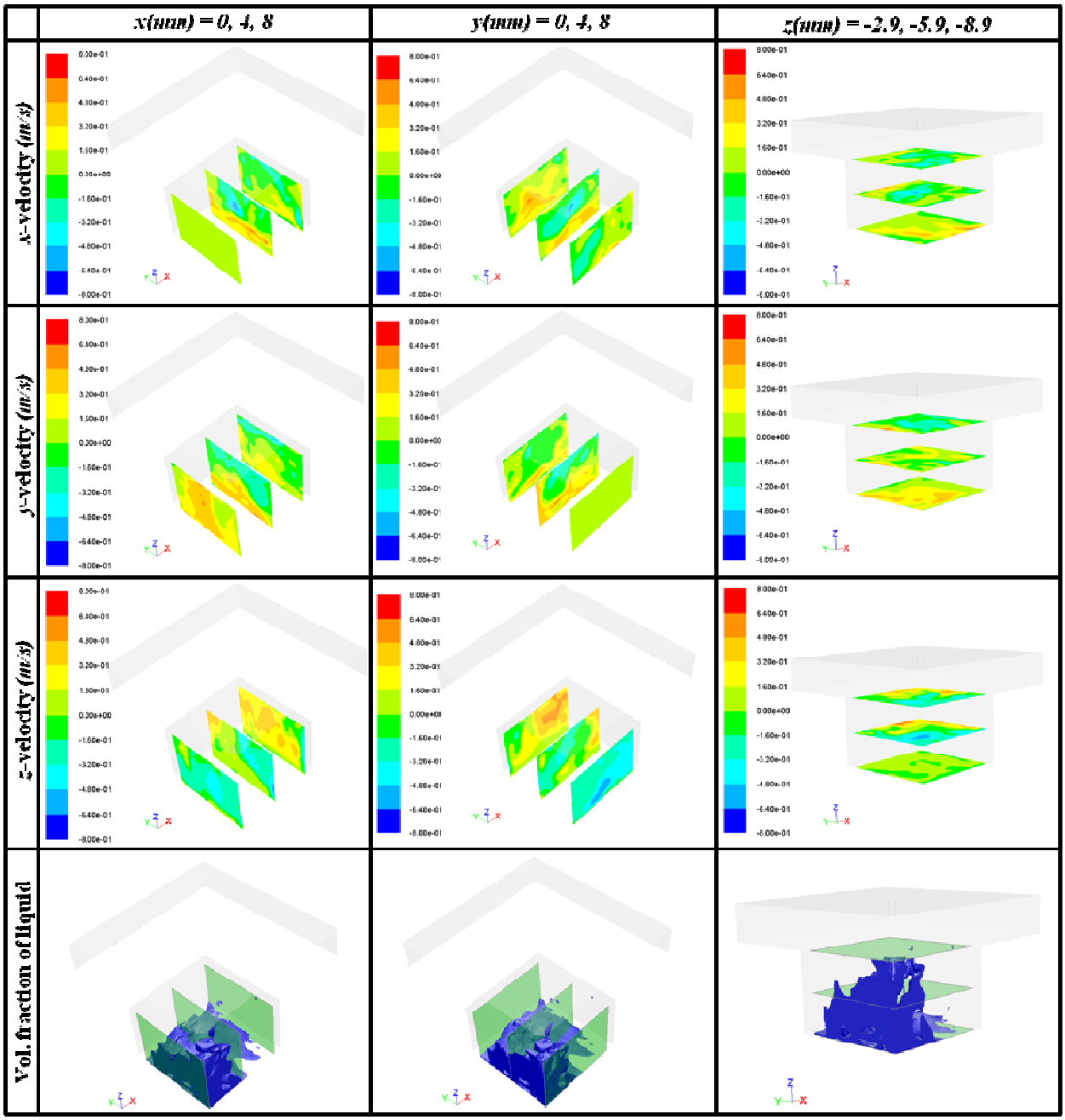

Figure 3.3.3: Contour of the components of velocity of the mixture and volume fraction of cell suspension (0.5 - 1) for -60 kPa initial vacuum pressure at time t = 0.2 seconds. The components of the velocity field on cross-sections perpendicular to the x-plane (x = 0mm, 4mm, 8mm), y-plane (y = 0mm, 4mm, 8mm) and z-plane (z = -2.9mm, -5.9mm, -8.9mm) and the corresponding volume fraction contour at time t = 0.20s.

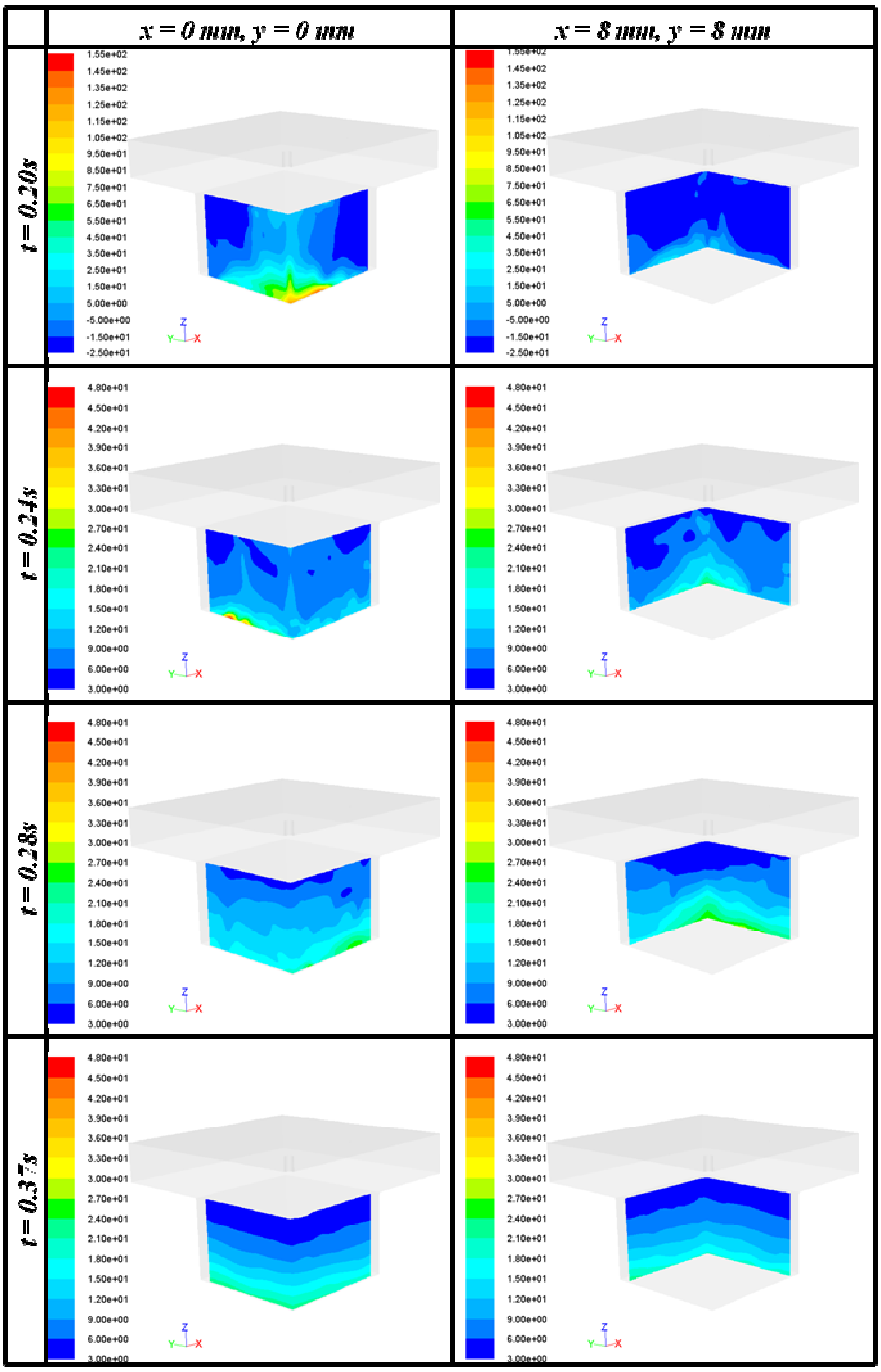

Figure 3.3.4: Static pressure distribution for -60 kPa initial gauge pressure. The static pressure contour on cross section parallel to the *x*-axis (*y* = 0mm, *y*= 8mm) and *y*- axis (*x* = 0mm, *x* = 8mm)

Table 3.3.1. Summary of results for initial vacuum pressure = -60 kPa on cross-sections parallel to the *y*-axis.

		Static pressure	**Velocity magnitude**	***x*-velocity**	***y*-velocity**	***z*-velocity**
		(*pa*)	**(*m/s*)**	**(*m/s*)**	**(*m/s*)**	**(*m/s*)**
t* = 0.20*s	max	141.58	0.6531	0.6418	0.6825	-0.5747
	min	-26.88	0.0181	-0.7071	-0.5788	0.7275
t* = 0.24*s	max	48.41	0.4740	0.3254	0.3613	0.3766
	min	3.96	7.40 e-03	-0.2396	-0.2942	-0.3853
t* = 0.28*s	max	28.18	0.2867	0.1672	0.2844	0.2551
	min	3.52	5.04 e-03	-0.1846	-0.1796	-0.2457
t* = 0.37*s	max	23.01	0.1453	0.0812	0.1197	0.1415
	min	3.02	2.14 e-03	-0.0786	-0.0751	-0.1205

Table 3.3.2. Summary of results for initial gauge pressure = -60 kPa on cross-sections parallel to the *x*-axis.

		Static pressure	**Velocity magnitude**	***x*-velocity**	***y*-velocity**	***z*-velocity**
		(*pa*)	**(*m/s*)**	**(*m/s*)**	**(*m/s*)**	**(*m/s*)**
t* = 0.20*s	max	140.40	0.6365	0.6418	0.6825	0.7275
	min	-20.31	0.0160	-0.7071	-0.5788	-0.5747
t* = 0.24*s	max	35.35	0.5051	0.3108	0.4052	0.4097
	min	3.96	3.51 e-03	-0.2533	-0.2139	-0.3853
t* = 0.28*s	max	27.63	0.2731	0.1632	0.1749	0.2122
	min	3.22	5.04 e-03	-0.1888	-0.1663	-0.2475
t* = 0.37*s	max	22.65	0.1564	0.0961	0.1117	0.1118
	min	2.73	6.08 e-04	-0.0700	-0.0974	-0.1504

Table 3.3.3. Summary of results for initial gauge pressure = -60 kPa on cross-sections parallel to the *x*-*y* plane.

		Static pressure	**Velocity magnitude**	***x*-velocity**	***y*-velocity**	***z*-velocity**
		(*pa*)	**(*m/s*)**	**(*m/s*)**	**(*m/s*)**	**(*m/s*)**
t* = 0.20*s	max	140.40	0.7942	0.5291	0.5473	0.7261
	min	-19.78	0.0160	-0.5320	-0.4504	-0.5571
t* = 0.24*s	max	48.41	0.4920	0.3919	0.4005	0.4555
	min	4.08	2.51 e-03	-0.2197	-0.2316	-0.3793
t* = 0.28*s	max	28.18	0.4336	0.2278	0.2671	0.3023
	min	2.17	5.04 e-03	-0.1700	-0.1923	-0.2299
t* = 0.37*s	max	23.02	0.1701	0.1000	0.1090	0.1316
	min	2.69	6.09 e-04	-0.0845	-0.0856	-0.1615

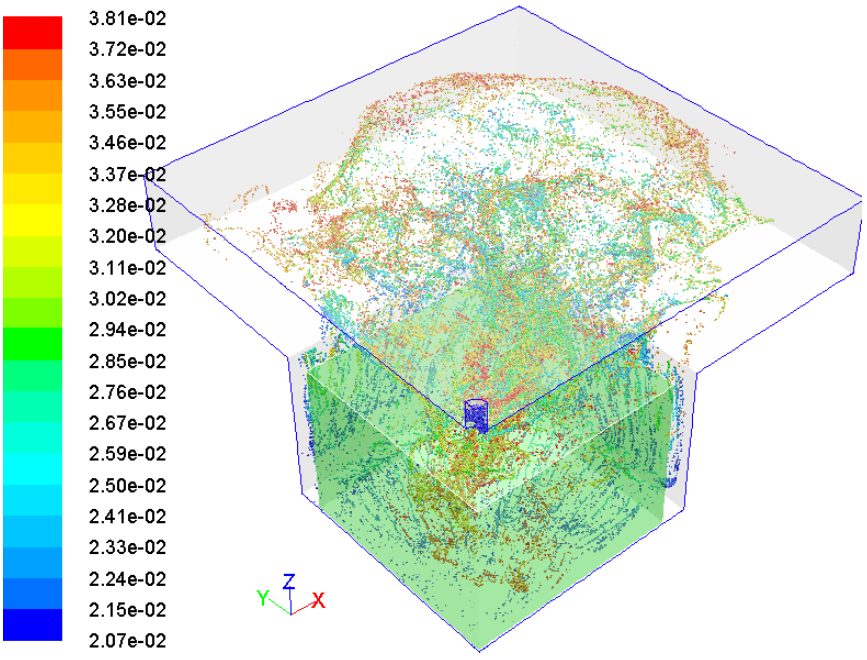

Figure 3.3.5: Distribution of the cells in the scaffold and cavity at *t* = 0.20 seconds for -60kPa initial vacuum pressure. The cells are colored by the residence time.

Furthermore, the observed spillage of the celll suspension into the upper chamber of the cavity in addition to the very low volume of cell suspension in the scaffold suggested the need to further reduce the initial vacuum presure in the cavity. To achieve this, at the beginning of the solution the cavity was patched with a guage pressure of -20 kPa. All other conditions were kept similar to the previous two cases. The simulation took 0.4 seconds to inject 0.25 ml of the cell suspension into the cavity. The initial flow rate was 8.03 e-04 *kg/s* at t = 1.0 e-03 seconds. Figure 3.4.1 showed that the flow of the cell suspension was limited to the lower chamber of the cavity for the entire duration of the flow. At time t = 2 seconds, 76% off the volume of the cell suspension was in the scaffold. This revealed a significant improvement in the amount of cell suspension in the scaffold and, potentially, the amount of cells seeded into the scaffold. In general, the fluid velocity was much smaller compared to the two previous cases. At time t = 0.46 seconds, small regions of higher velocities were identified on the top right hand corner of one of cross sections parallel to the y- axis (x = 0mm), top left hand corner of one of the cross section parallel to the x –axis (y = 0mm) and on the top section of the cross-sections parallel to the x-y plane. Elsewhere the velocities appeared very low. When these regions with higher velocities were cross referenced with identical regions on figure 3.4.3, it was observed that these velocities were in the negative z-direction (table 3.3.4), indicating the flow of fluid into these regions. It is noteworthy that the different components of the velocities showed less variation. Thus, indicating uniform flow in all directions. Figure 3.4.5 reports a better seeding of the scaffold. Majority of the cells were seeded into the scaffold.

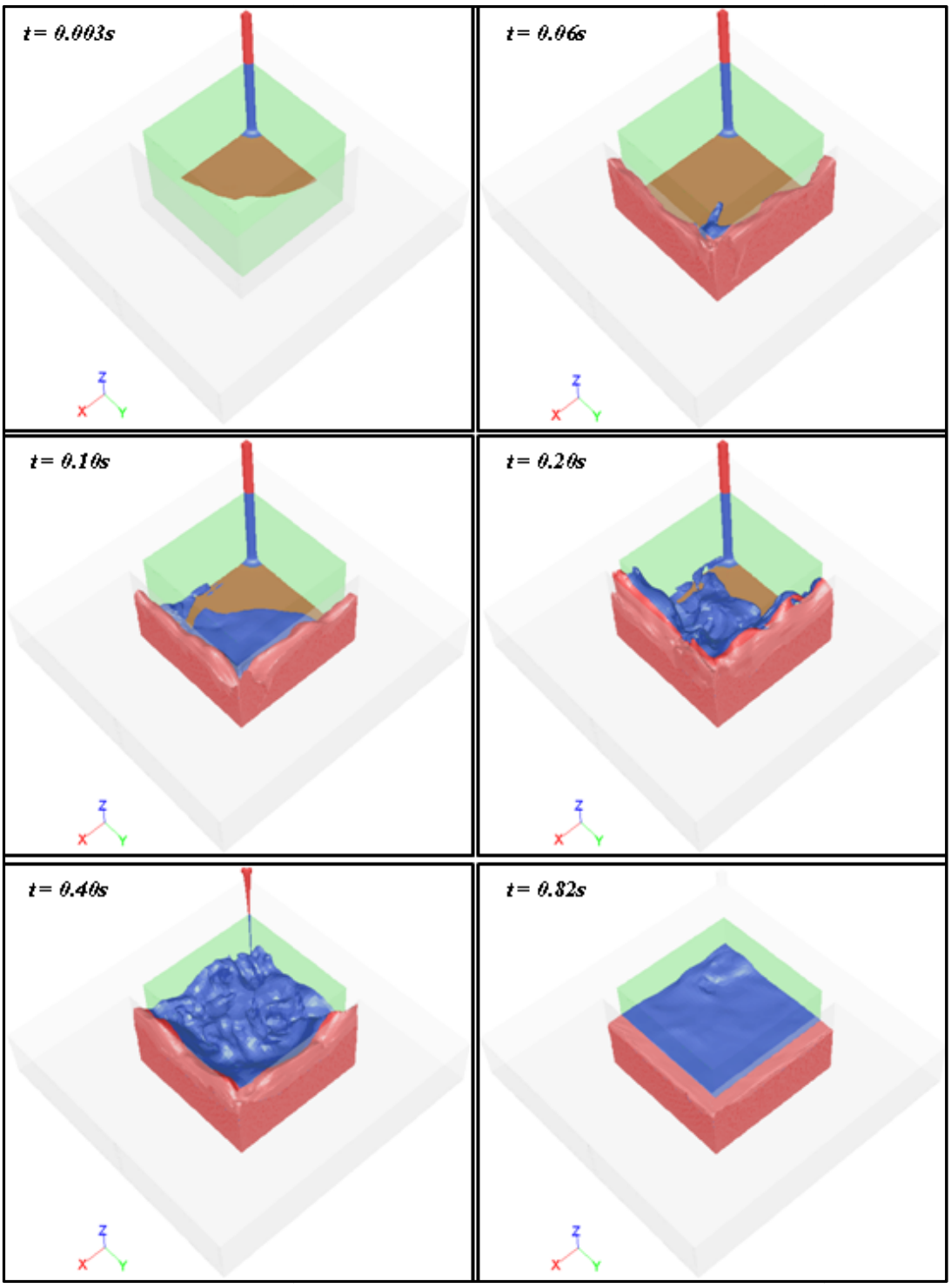

Figure 3.3.6: Liquid phase volume fraction (0.5 -1.0) distribution in the scaffold- cavity assembly after 0.67 seconds for -20k initial vacuum pressure. Blue color indicates the fraction of the liquid phase that is in the scaffold and the red color indicates the fraction of the liquid that is not in the scaffold.

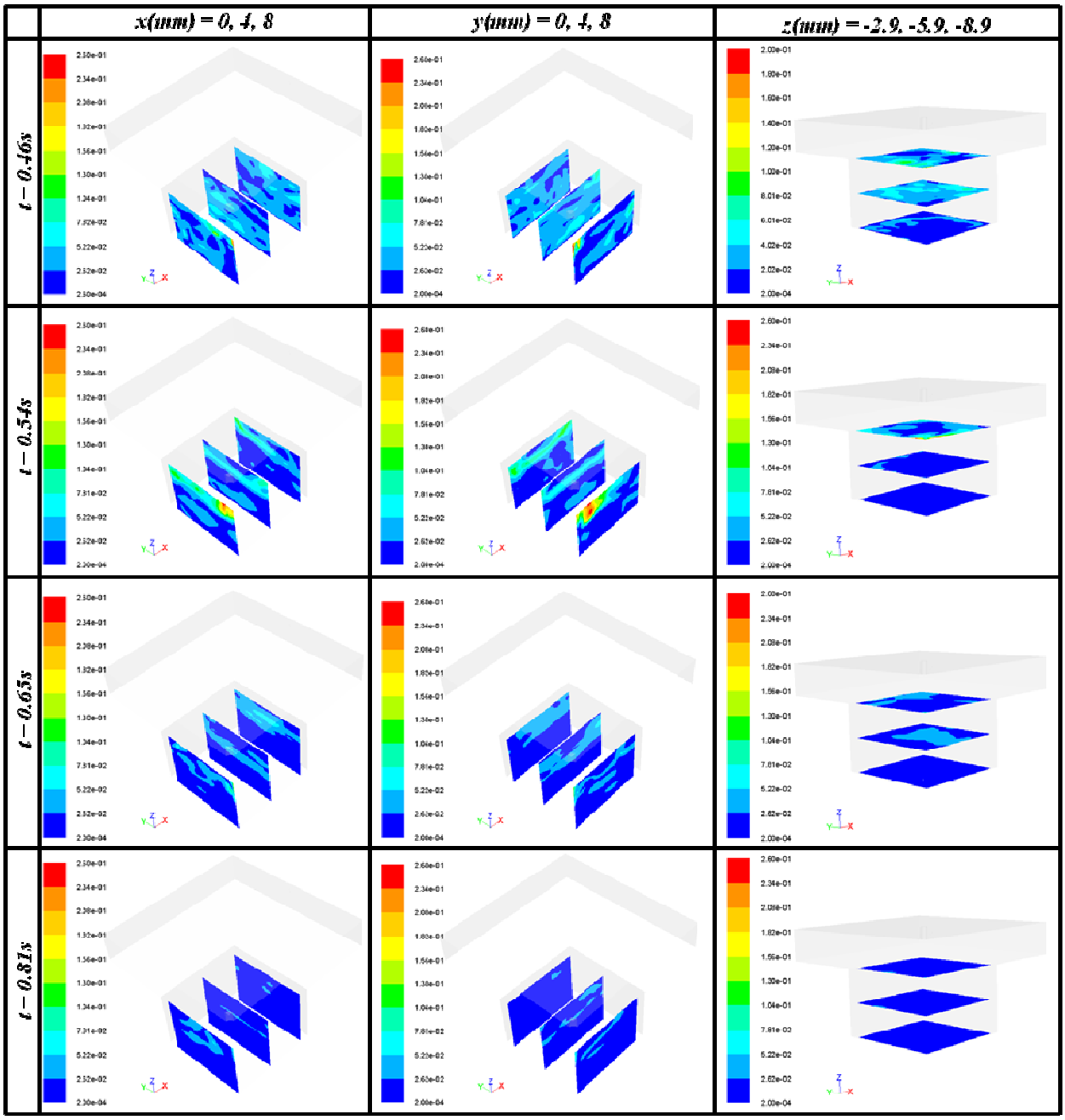

Figure 3.3.7: Velocity magnitude distribution for -20 kPa initial vacuum pressure. The velocity field on cross-sections perpendicular to the *x*-plane (*x* = 0mm, 4mm, 8mm), *y*-plane (*y* = 0mm, 4mm, 8mm) and *z*-plane (*z* = -2.9mm, -5.9mm, -8.9mm) at time *t* = 0.46s, 0.54s, 0.65s and 0.81s.

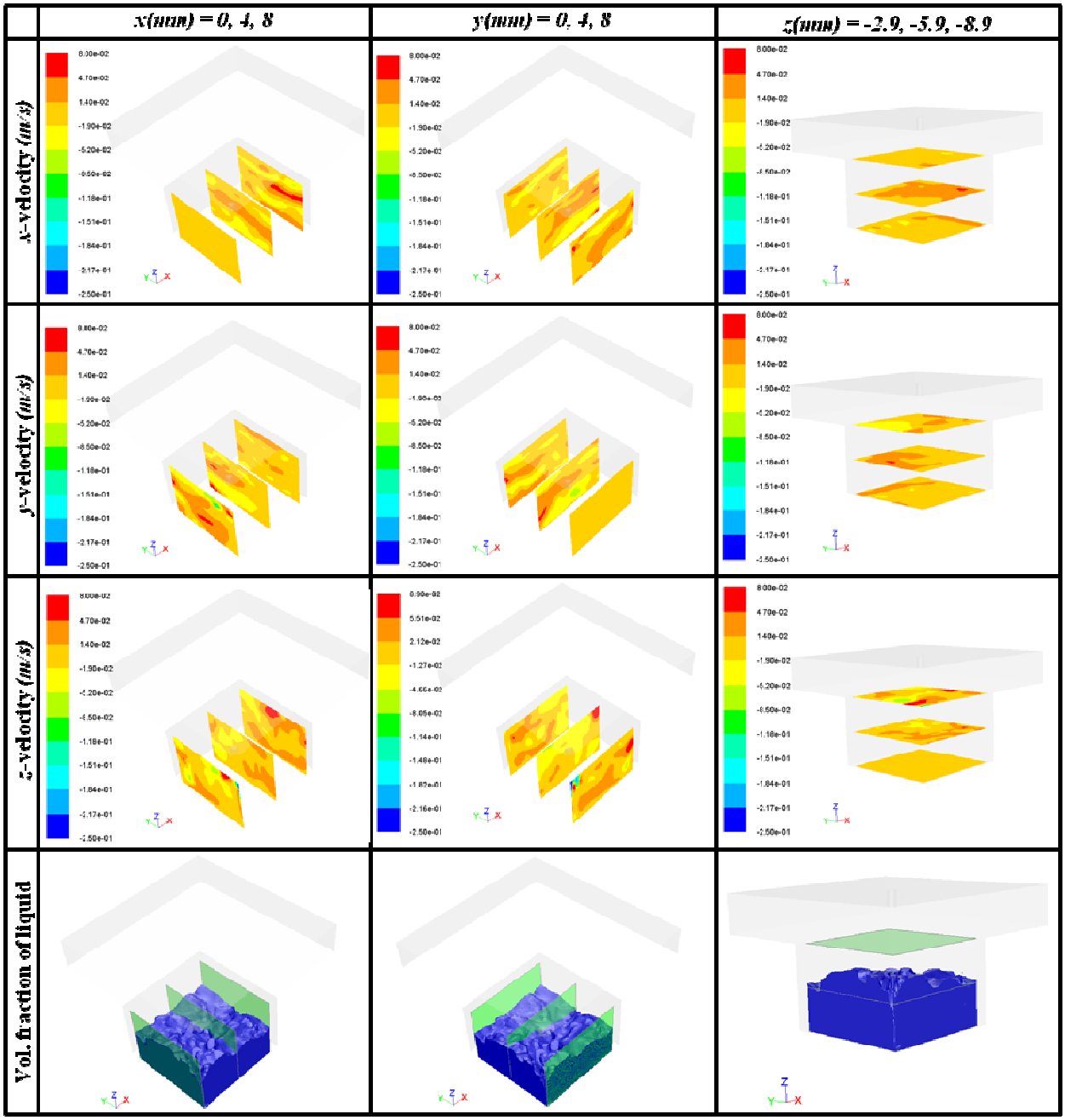

Figure 3.3.8: Contour of the components of velocity of the mixture and volume fraction of cell suspension (0.5 - 1) for -20 kPa initial vacuum pressure at time t = 0.46 seconds. The components of the velocity field on cross-sections perpendicular to the x-plane (x = 0mm, 4mm, 8mm), y-plane (y = 0mm, 4mm, 8mm) and z-plane (z = -2.9mm, -5.9mm, -8.9mm) and the corresponding volume fraction contour at time t = 0.46s.

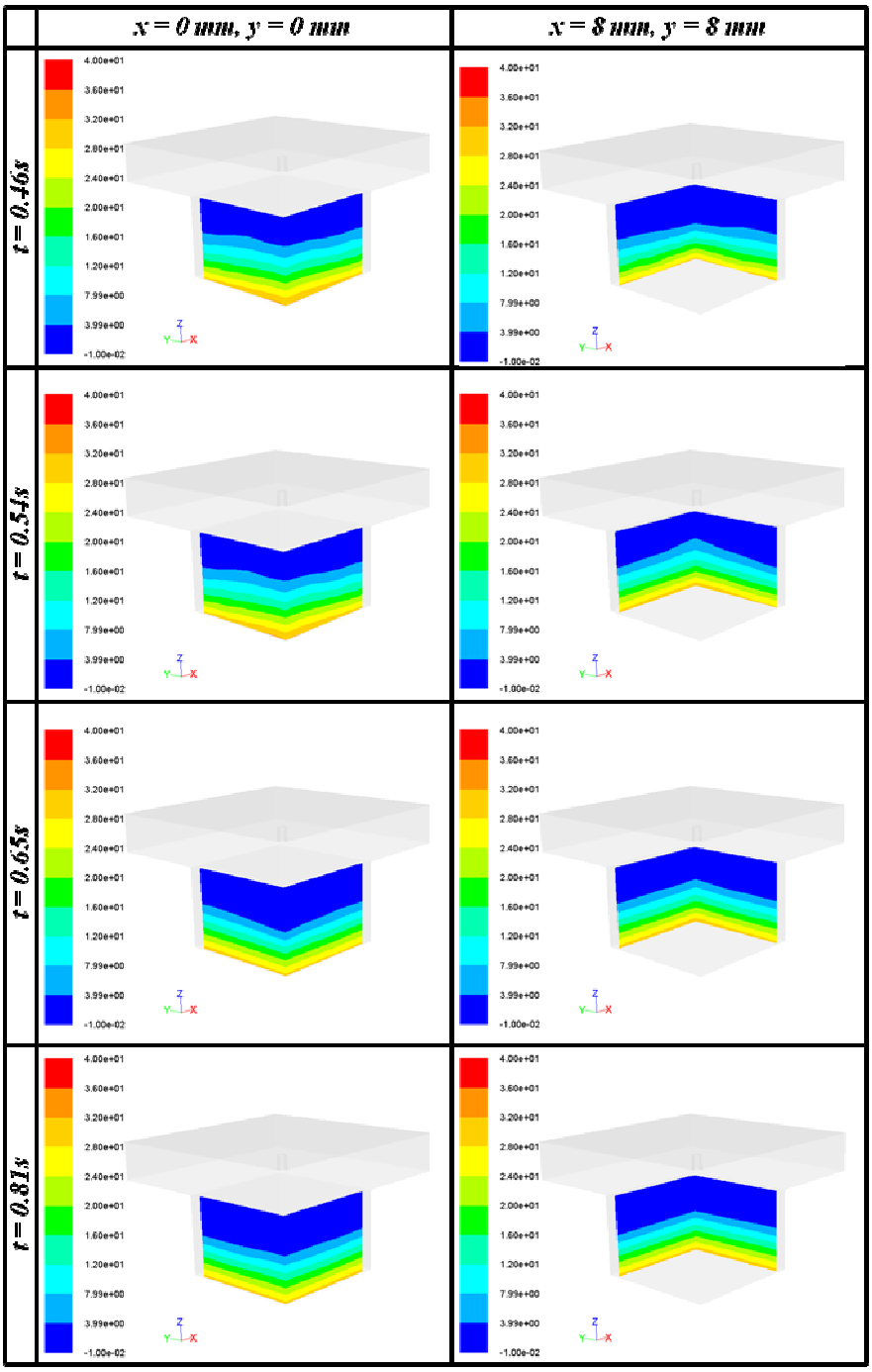

Figure 3.3.9: Static pressure distribution for -20kPa initial gauge pressure. The static pressure contour on cross section parallel to the *x*-axis (*y* = 0mm, *y*= 8mm) and *y*- axis (*x* = 0mm, *x* = 8mm)

Table 3.3.4. Summary of results for initial gauge pressure = -20kPa on cross-sections parallel to the *y*-axis.

		Static pressure	**Velocity magnitude**	***x*-velocity**	***y*-velocity**	***z*-velocity**
		(*pa*)	**(*m/s*)**	**(*m/s*)**	**(*m/s*)**	**(*m/s*)**
t* = 0.46*s	max	32.67	0.2487	0.0578	0.0740	0.0806
	min	0.15	8.48 e-04	-0.0539	-0.1531	-0.2487
t* = 0.54*s	max	30.84	0.2570	0.0769	0.0502	0.2566
	min	-0.06	6.81 e-04	-0.0834	-0.0822	-0.1095
t* = 0.65*s	max	30.92	0.1344	0.0336	0.0639	0.0959
	min	0.08	1.65 e-04	-0.0453	-0.0490	-0.1344
t* = 0.81*s	max	30.31	0.0658	0.0272	0.0385	0.0303
	min	0.03	3.33 e-04	-0.0217	-0.0283	-0.0658

Table 3.3.5. Summary of results for initial gauge pressure = -20kPa on cross-sections parallel to the *x*-axis.

		Static pressure	**Velocity magnitude**	***x*-velocity**	***y*-velocity**	***z*-velocity**
		(*pa*)	**(*m/s*)**	**(*m/s*)**	**(*m/s*)**	**(*m/s*)**
t* = 0.46*s	max	32.44	0.2487	0.0674	0.0553	0.0892
	min	0.16	1.38 e-03	-0.0561	-0.0592	-0.2487
t* = 0.54*s	max	30.84	0.2691	0.1894	0.0438	0.2639
	min	-0.07	1.86 e-04	-0.1035	-0.0670	-0.1121
t* = 0.65*s	max	30.95	0.1344	0.0440	0.0605	0.0747
	min	0.08	1.65 e-04	-0.0512	-0.0405	-0.1344
t* = 0.81*s	max	30.31	0.0658	0.0309	-0.0251	0.0311
	min	0.03	3.75 e-04	-0.0283	0.0319	-0.0658

Table 3.3.6. Summary of results for initial gauge pressure = -20kPa on cross-sections parallel to the *x*-*y* plane.

		Static pressure	**Velocity magnitude**	***x*-velocity**	***y*-velocity**	***z*-velocity**
		(*pa*)	**(*m/s*)**	**(*m/s*)**	**(*m/s*)**	**(*m/s*)**
t* = 0.46*s	max	32.67	0.2270	0.0567	0.0521	0.0822
	min	0.15	8.35 e-04	-0.0309	-0.0583	-0.2270
t* = 0.54*s	max	30.84	0.2691	0.0875	0.0412	0.2639
	min	-0.07	2.74 e-04	-0.0544	-0.0636	-0.1010
t* = 0.65*s	max	30.95	0.1344	0.0264	0.0346	0.0449
	min	0.08	1.70 e-04	-0.0389	-0.0351	-0.1344
t* = 0.81*s	max	30.30	0.0635	0.0165	0.0259	0.0171
	min	0.03	1.92 e-04	-0.0146	-0.0199	-0.0635

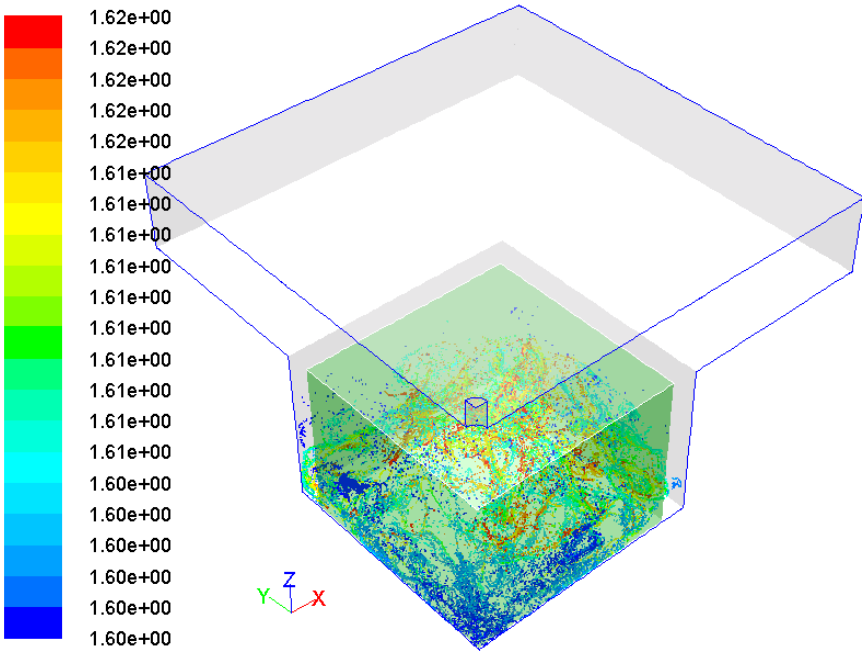

Figure 3.3.10: Distribution of the cells in the scaffold and cavity at *t* = 2 seconds for -20 kPa initial vacuum pressure. The cells are colored by the residence time.

3.4 Transient Profile in cylindrical Scaffold-Cavity Assembly Using Determined Optimal Initial Vacuum Pressure

To demonstrate the broad applicability of the determined optimal initial vacuum pressure, another transient VOF CFD simulation was carried out on a cylindrical configuration of the seeding device (figure 3.4.1) Results from this new simulation were consistent with the cubic configuration. Though there was minimal spillage into the upper chamber of the cavity, 72% of the volume of the cell suspension was in the scaffold (figure 3.4.2). It took 0.33 seconds for 0.25 ml of the cell suspension to be injected in the cavity. The initial mass flow rate at 0.01 seconds is 7.93 kg/s. Figure 3.4.3 showed the position and the residence time of the cells in the seeding device. Has it can be observed, majority of the cells were located in the scaffold and the motion of the cells is towards the upper region of the scaffold predicting better uniform seeding at later time points. These observations demonstrate the robustness of the -20 kPa initial vacuum pressure for the seeding device.

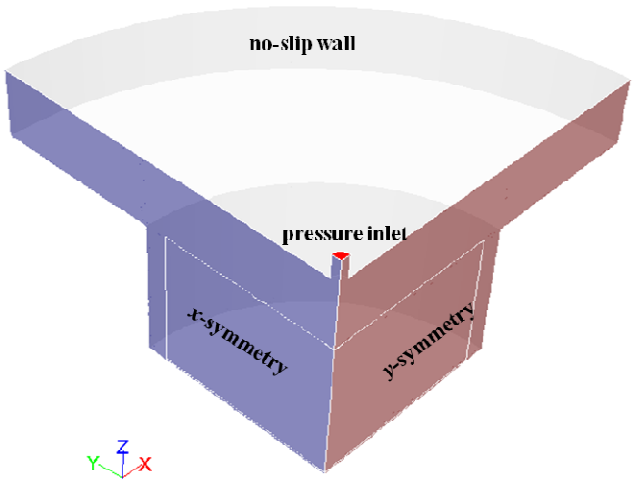

Figure 3.4.1: Cylindrical scaffold-cavity assembly boundary conditions

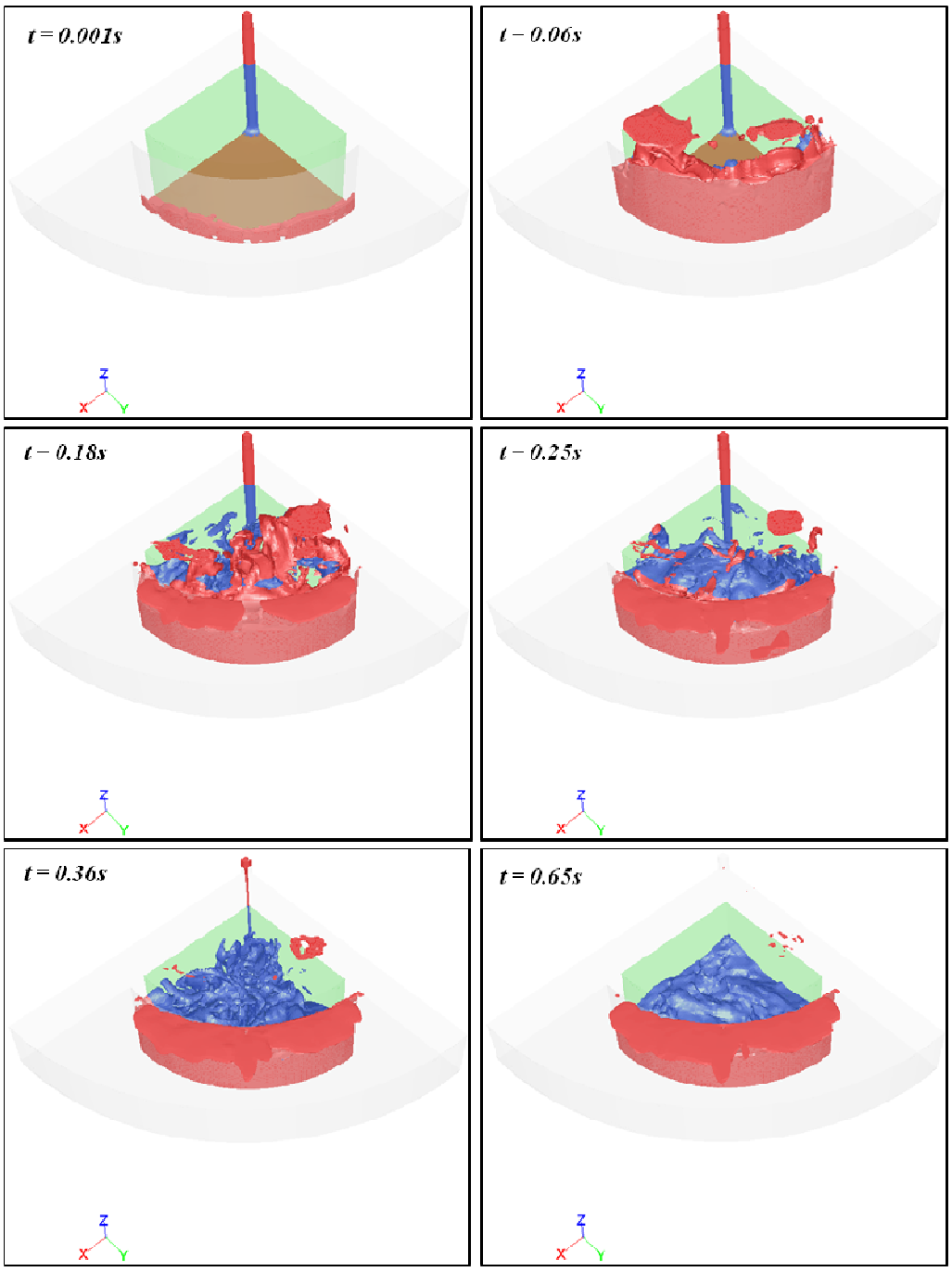

Figure 3.4.2: Liquid phase volume fraction (0.5 -1.0) distribution in the cylindrical scaffold-cavity assembly after 0.65 seconds for -20kPa initial vacuum pressure. Blue color indicates the fraction of the liquid phase that is in the scaffold and the red color indicates the fraction of the liquid that is not in the scaffold

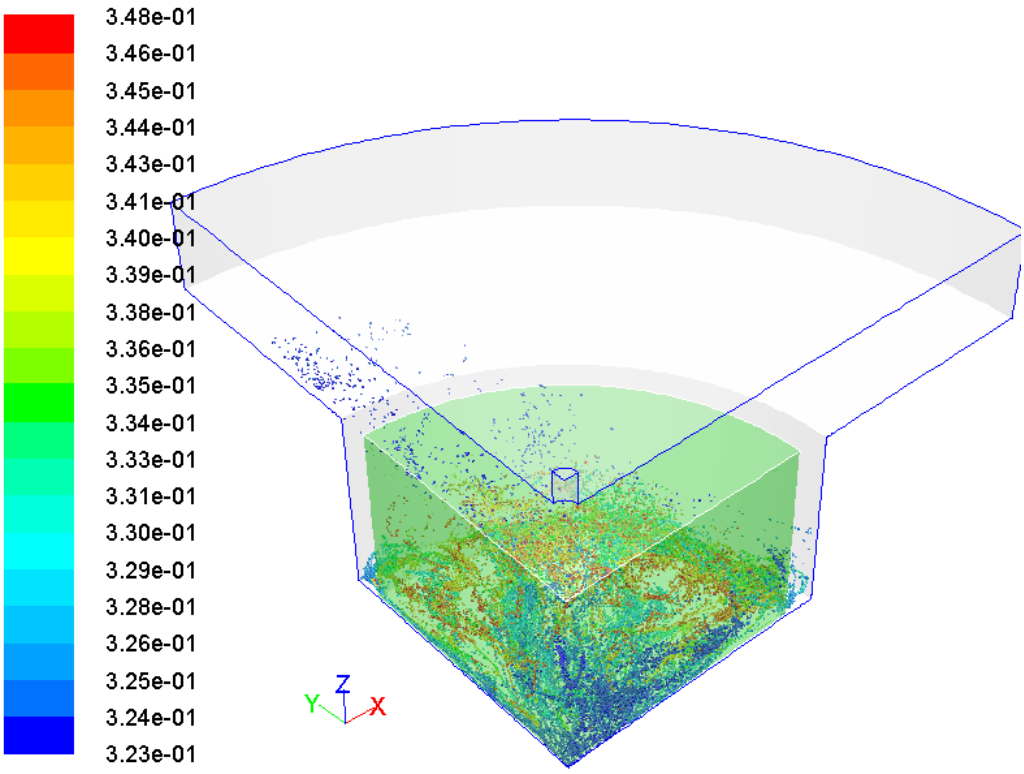

Figure 3.4.3: Distribution of the cells in the cylindrical scaffold and cavity at t = 0.65 seconds for -20kPa initial vacuum pressure. The cells are colored by the residence time.

DISCUSSION

One of the challenges faced by tissue engineers is developing efficient cell seeding technique and technology. The seeding of porous scaffold is a fundamental step in engineering tissue constructs that are clinically viable. One of the critical issue in this step involve understanding how to uniformly seed the cells into the scaffold to promote rapid and full thickness tissue formation and remodeling. There are also a variety of technical challenges such as creating a technology that is suitable for a surgical environment, user independent and able to fabricate tissue construct in a highly reproducible manner.

To address these challenges, one approach has involved designing a seeding device that load cells into the porous scaffold by inducing continuous oscillatory fluid flow through the scaffold pores [42]. Though higher seeding efficiency was obtained in this approach, but the use of this technique in a surgical environment that requires timely seeding of the cells into the porous scaffold is questionable. Recently a new seeding technique has been investigated, and is based on combining the synergistic action of vacuum, rotation, and flow to seed cells into the scaffold [31]. However, this technique is limited to hollow tubular tissue construct and has not been optimized for different types of scaffold.

The aims of this study were to use numerical methods to characterize the seeding efficiency of a pre-existing seeding technology that utilizes fluid flow induced by vacuum, since fluid flow provides an ideal means of transporting the cells into the scaffold and optimize the seeding technique. Subsequently, applying the detailed information obtained from the numerical study to design an optimized novel compact cell seeding technology is feasible.

To establish the quantitative relationships between the cell seeding efficiency of the technique with the initial vacuum pressure a CFD model for the seeding device was developed. The

extreme complexity of the scaffold architecture – pores and interconnecting channels – and volume blockages that was physically present were excluded in the CFD model. The main assumption is that the fluid flow through the porous scaffold obeys Darcy's law. The grid representing the computational domain was refined to check for grid independent solution. In other to provide justification for modeling a quarter of the geometry as supposed to the full geometry, a preliminary study was performed to investigate the presence of symmetry. It was determined that symmetry existed on a quarter cross-section of the geometry.

Results from the study showed that inefficient seeding of the cells into the scaffold was obtained when the recommended initial vacuum pressure (-100 kPa) was used. A large portion of the cell suspension spilt into the upper chamber of the cavity and only 40% of the volume of the cell suspension was in the porous scaffold. The result suggested the need to further decrease the vacuum pressure in other to prevent the spill. To address this need, the initial vacuum pressure was decreased to -60kPa and a similar simulation was performed. Results for the new case revealed very little improvement in the seeding efficiency (48% of the volume of the cell suspension was in the porous scaffold). Further decrease in the initial vacuum pressure to -20kPa yielded more adequate and optimal seeding efficiency (76% of the volume of the cell suspension was in the porous scaffold). Similar result was obtained when the -20 kPa initial pressure was applied to a cylindrical configuration of the seeding device. In general, the two configurations of the seeding device – cubic and cylindrical – were more optimal to homogeneous seeding of the porous scaffold at -20kPa than higher initial vacuum pressure.

Taken together, the results indicated that the initial vacuum pressure has a major impact on the fluid flow in the seeding device cavity and thereby on the homogeneous seeding of the porous scaffold. Hence the design of an optimal seeding device that uses vacuum induced fluid flow

techniques must take into account the interplay of the initial vacuum pressure and the fluid flow in the cavity or chamber of the seeding device.

CONCLUSION AND RECOMMENDATIONS

This study addressed the problem of inhomogeneous seeding of stem cells in a novel seeding device and technique. Computational fluid dynamic tools were used to characterize and determined the fluid flow in the device and the optimal initial vacuum pressure for efficient cell seeding respectively. Numerical method is extremely useful in understanding the implications of fluid flow on seeding efficiency of tissue engineering seeding devices and provides insight into the design and optimization of such devices.

Data from the CFD simulation suggested that an initial vacuum pressure of -20kPa was optimal for effective seeding of a cubic and cylindrical configuration of the seeding device. It is expected that the 3-D model presented in this study will be employed as part of a systemic stepwise approach useful in the optimization of cell seeding techniques and corresponding technology. It is noteworthy to consider the following limitations in this study: Firstly, this study lacks an experimental validation of the results obtained from the CFD simulation. Although *in vitro* and *in vivo* experiments are necessary, numerical analysis provided in this study is still very useful in reducing the numerous and expensive experiments that will otherwise be performed. Thus, time and resources will be saved. The second limitation was the check for grid independence suggested that the solution has not fully reached grid independence. The computational cost to significantly reduce this error is very high. However, for this study such error could be ignored since the objective of this study was to optimize the cell seeding efficiency and not to determine the exact location of the cells in the scaffold. Furthermore, future work will be required to address the above-mentioned limitations.

REFERENCES

1. Vacanti, J. P. and R. Langer (1999). "Tissue engineering: the design and fabrication of living replacement devices for surgical reconstruction and transplantation." Lancet 354 Suppl 1: SI32-4.

2. Bisceglie, V. (1933). Uber die antineoplastische immunitat; heterologe einpflanzung von Tumoren in Huhner-embryonen. Ztschr. Krebsforsch. 40: 122-140

3. Knazek, R. A., P. M. Gullino, et al. (1972). "Cell culture on artificial capillaries: an approach to tissue growth in vitro." Science 178(56): 65-6.

4. Chick, W. L., A. A. Like, et al. (1975). "Beta cell culture on synthetic capillaries: an artificial endocrine pancreas." Science 187(4179): 847-9

5. Bell, E., H. P. Ehrlich, et al. (1981). "Living tissue formed in vitro and accepted as skin-equivalent tissue of full thickness." Science 211(4486): 1052-4.

6. Burke, J. F., I. V. Yannas, et al. (1981). "Successful use of a physiologically acceptable artificial skin in the treatment of extensive burn injury." Ann Surg 194(4): 413-28.

7. Vacanti, J. P., M. A. Morse, et al. (1988). "Selective cell transplantation using bioabsorbable artificial polymers as matrices." J Pediatr Surg 23(1 Pt 2): 3-9.

8. Olivares, A. L., E. Marsal, et al. (2009). "Finite element study of scaffold architecture design and culture conditions for tissue engineering." Biomaterials 30(30): 6142-9.

9. Hutmacher, D. W., M. Sittinger, et al. (2004). "Scaffold-based tissue engineering: rationale for computer-aided design and solid free-form fabrication systems." Trends Biotechnol 22(7): 354-62.

10. Atala, A. (2004). "Tissue engineering and regenerative medicine: concepts for clinical application." Rejuvenation Res 7(1): 15-31.

11. Langer, R. and J. P. Vacanti (1993). "Tissue engineering." Science 260(5110): 920-6.

12. Mazariegos, G. V., J. F. Patzer, 2nd, et al. (2002). "First clinical use of a novel bioartificial liver support system (BLSS)." Am J Transplant 2(3): 260-6.

13. Griffith, L. G. and G. Naughton (2002). "Tissue engineering--current challenges and expanding opportunities." Science 295(5557): 1009-14.

14. Williams, D. F. (2006). "To engineer is to create: the link between engineering and regeneration." Trends Biotechnol 24(1): 4-8.

15. El-Ghannam, A. (2005). "Bone reconstruction: from bioceramics to tissue engineering." Expert Rev Med Devices 2(1): 87-101.

16. Mauney, J. R., V. Volloch, et al. (2005). "Role of adult mesenchymal stem cells in bone tissue engineering applications: current status and future prospects." Tissue Eng 11(5-6): 787-802.

17. Mistry, A. S. and A. G. Mikos (2005). "Tissue engineering strategies for bone regeneration." Adv Biochem Eng Biotechnol 94: 1-22.

18. Hunziker, E. B. (2002). "Articular cartilage repair: basic science and clinical progress. A review of the current status and prospects." Osteoarthritis Cartilage 10(6): 432-63.

19. Oreffo, R. O., C. Cooper, et al. (2005). "Mesenchymal stem cells: lineage, plasticity, and skeletal therapeutic potential." Stem Cell Rev 1(2): 169-78.

20. Porter, B., R. Zauel, et al. (2005). "3-D computational modeling of media flow through scaffolds in a perfusion bioreactor." J Biomech 38(3): 543-9.

21. Hutmacher, D. W. (2000). "Scaffolds in tissue engineering bone and cartilage." Biomaterials 21(24): 2529-43.

22. Boschetti, F., M. T. Raimondi, et al. (2006). "Prediction of the micro-fluid dynamic environment imposed to three-dimensional engineered cell systems in bioreactors." J Biomech 39(3): 418-25.

23. Holy, C. E., M. S. Shoichet, et al. (2000). "Engineering three-dimensional bone tissue in vitro using biodegradable scaffolds: investigating initial cell-seeding density and culture period." J Biomed Mater Res 51(3): 376-82.

24. Freed, L. E., A. P. Hollander, et al. (1998). "Chondrogenesis in a cell-polymer-bioreactor system." Exp Cell Res 240(1): 58-65.

25. Ishaug-Riley, S. L., G. M. Crane-Kruger, et al. (1998). "Three-dimensional culture of rat calvarial osteoblasts in porous biodegradable polymers." Biomaterials 19(15): 1405-12.

26. Kim, B. S., A. J. Putnam, et al. (1998). "Optimizing seeding and culture methods to engineer smooth muscle tissue on biodegradable polymer matrices." Biotechnol Bioeng 57(1): 46-54.

27. Freed, L. E., R. Langer, et al. (1997). "Tissue engineering of cartilage in space." Proc Natl Acad Sci U S A 94(25): 13885-90.

28. Carrier, R. L., M. Papadaki, et al. (1999). "Cardiac tissue engineering: cell seeding, cultivation parameters, and tissue construct characterization." Biotechnol Bioeng 64(5): 580-9.

29. Naughton, G. K. (2002). "From lab bench to market: critical issues in tissue engineering." Ann N Y Acad Sci 961: 372-85.

30. Ratcliffe, A. and L. E. Niklason (2002). "Bioreactors and bioprocessing for tissue engineering." Ann N Y Acad Sci 961: 210-5.

31. Soletti, L., A. Nieponice, et al. (2006). "A seeding device for tissue engineered tubular structures." Biomaterials 27(28): 4863-70.

32. Carter, J., K. Hristova, et al. (2003). "Short exposure time sensitivity of white cells to shear stress." Asaio J 49(6): 687-91.

33. Dardik, A., L. Chen, et al. (2005). "Differential effects of orbital and laminar shear stress on endothelial cells." J Vasc Surg 41(5): 869-80.

34. Matsumura, G., N. Hibino, et al. (2003). "Successful application of tissue engineered vascular autografts: clinical experience." Biomaterials 24(13): 2303-8.

35. Remuzzi, A., S. Mantero, et al. (2004). "Vascular smooth muscle cells on hyaluronic acid: culture and mechanical characterization of an engineered vascular construct." Tissue Eng 10(5-6): 699-710.

36. Martin, I., D. Wendt, et al. (2004). "The role of bioreactors in tissue engineering." Trends Biotechnol 22(2): 80-6

37. Bruinink, A., D. Siragusano, et al. (2001). "The stiffness of bone marrow cell-knit composites is increased during mechanical load." Biomaterials 22(23): 3169-78.

38. Li, Y., T. Ma, et al. (2001). "Effects of filtration seeding on cell density, spatial distribution, and proliferation in nonwoven fibrous matrices." Biotechnol Prog 17(5): 935-44.

39. Xiao, Y. L., J. Riesle, et al. (1999). "Static and dynamic fibroblast seeding and cultivation in porous PEO/PBT scaffolds." J Mater Sci Mater Med 10(12): 773-7.

40. Vunjak-Novakovic, G., B. Obradovic, et al. (1998). "Dynamic cell seeding of polymer scaffolds for cartilage tissue engineering." Biotechnol Prog 14(2): 193-202.

41. Burg, K. J., M. Delnomdedieu, et al. (2002). "Application of magnetic resonance microscopy to tissue engineering: a polylactide model." J Biomed Mater Res 61(3): 380-90.

42. Wendt, D., A. Marsano, et al. (2003). "Oscillating perfusion of cell suspensions through three-dimensional scaffolds enhances cell seeding efficiency and uniformity." Biotechnol Bioeng 84(2): 205-14.

43. Porter, B., R. Zauel, et al. (2005). "3-D computational modeling of media flow through scaffolds in a perfusion bioreactor." J Biomech 38(3): 543-9.

44. Cioffi, M., F. Boschetti, et al. (2006). "Modeling evaluation of the fluid-dynamic microenvironment in tissue-engineered constructs: a micro-CT based model." Biotechnol Bioeng 93(3): 500-10.

45. Sandino, C., J. A. Planell, et al. (2008). "A finite element study of mechanical stimuli in scaffolds for bone tissue engineering." J Biomech 41(5): 1005-14.

46. Sucosky, P., D. F. Osorio, et al. (2004). "Fluid mechanics of a spinner-flask bioreactor." Biotechnol Bioeng 85(1): 34-46.

47. Hutmacher, D. W. and H. Singh (2008). "Computational fluid dynamics for improved bioreactor design and 3D culture." Trends Biotechnol 26(4): 166-72.

48. Grimm, M. J. and J. L. Williams (1997). "Measurements of permeability in human calcaneal trabecular bone." J Biomech 30(7)

APPENDICES

Appendix A

Grid Independence

Cubic configuration

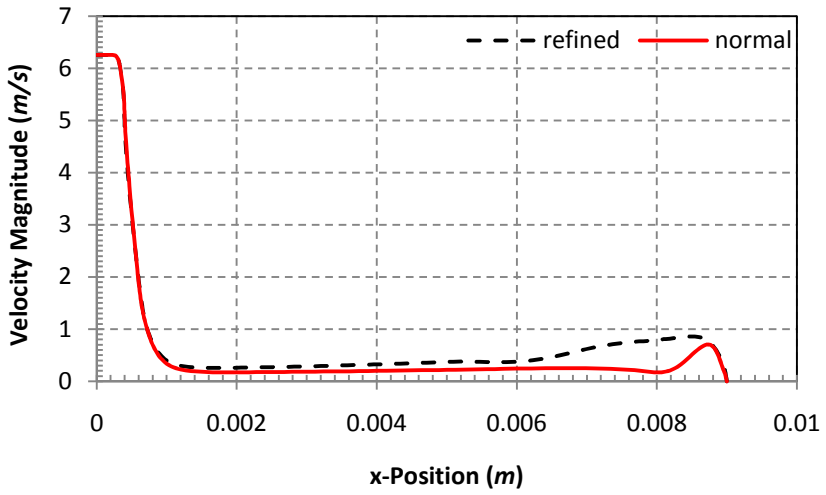

Figure A.1.1: Plot of velocity magnitude (*m/s*) vs. x-position (*m*) on a centerline parallel to the x-axis for normal and refined mesh at t = 0.0094 seconds.

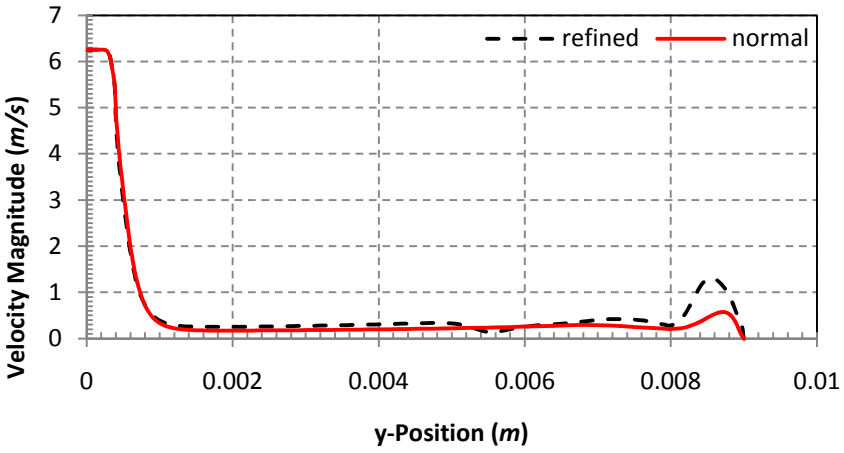

Figure A.1.2: Plot of velocity magnitude (*m/s*) vs. y-position (*m*) on a centerline parallel to the y-axis for normal and refined mesh at t = 0.0094 seconds.

Appendix B

Using FLUENT in ANSYS 12.1

Preparation

1. Copy mesh file (*mymesh.msh.gz*) to your working folder
2. **Start > Programs > ANSYS 12.1 > Fluid dynamics > click on FLUENT**
3. FLUENT launcher will pop up

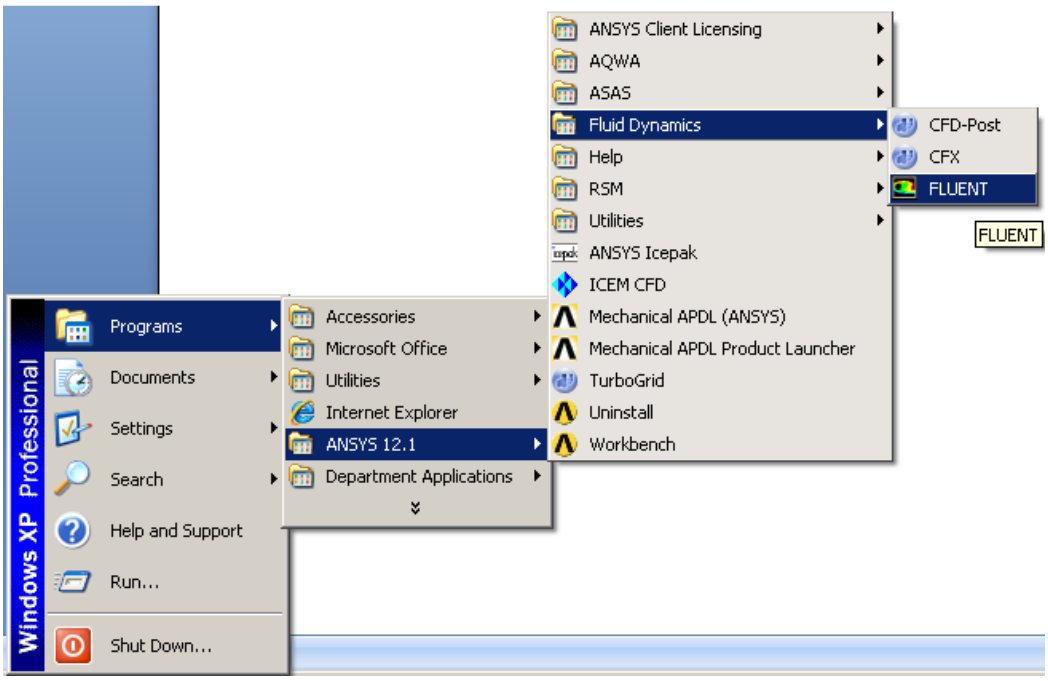

4. In the FLUENT launcher , start the 3D double precision version of ANSYS FLUENT
   (a) Select **3D** from **dimension** list
   (b) Enable **double precision**
   (c) Select your working folder from **working directory**

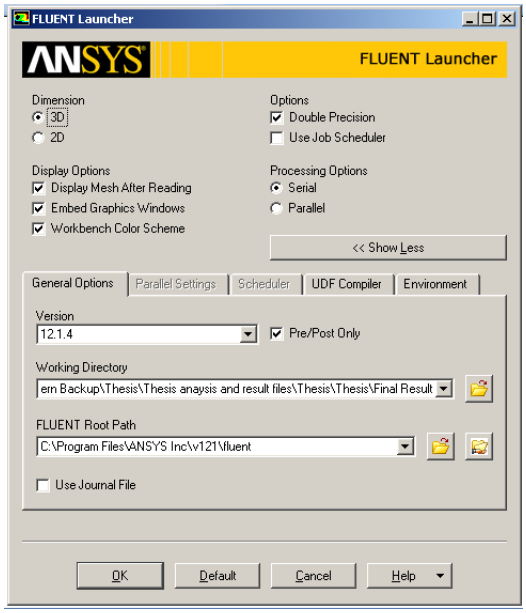

Step 1: Mesh

5. Read the mesh file (*mymesh.msh.gz*).

   File > Read > Mesh…

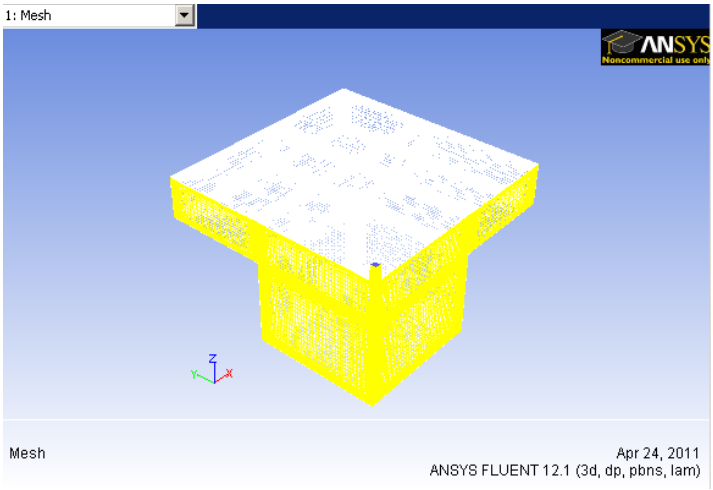

Step 2: General Settings

6. Define the solver settings

   General > Transient

7. Check the mesh

   General > check

8. Scale the mesh using a scale factor of 0.001 in the X, Y, and Z directions.

   General > scale

9. Reorder the domain until the bandwidth reduction is of the order of 0.1.

   Mesh > Reorder > Domain

Step 3: Models

10. Define the multiphase model
    Models > Multiphase > Edit…

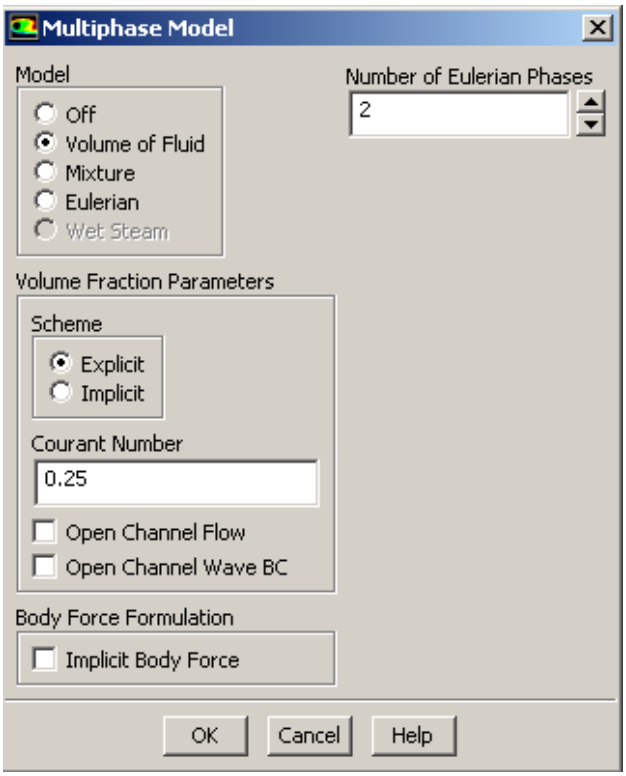

(a) Select **Volume of Fluid** from **Mode**l list.
(b) Enable the **Implicit Body Force**.
(c) Click **OK** to close the **Multiphase Model** dialog box

11. Define discrete phase.

    Models > Discrete Phase > Edit…

(a) Enable the **Interaction with Continuous Phase**.
(b) Click the **Tracking** tab and enter *500* for **Max. Number of Steps.**

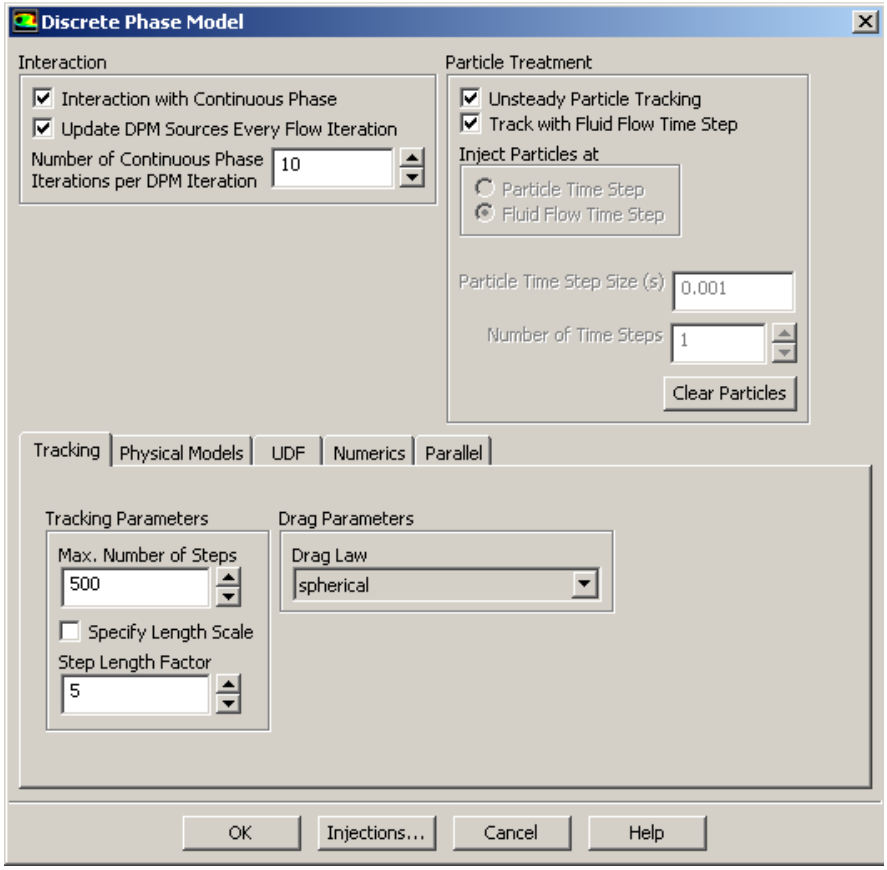

(c) Click on the **Injections…** to open the **Injections** dialog box.

(i) Click the **Create** button to open the **Set Injection Properties** dialog box.
(ii) Select **Surface** from the **Injection Type** drop-down list.
(iii) Select **Inlet** from **Release from Surfaces** drop-down list.
(iv) Select **Wood** from the **Material** drop-down list.
(v) Enter the following values in the Point Properties tab:

Parameter	**Value**
Diameter (m)	6e -06
Start Time(s)	0
Stop Time(s)	0.40
Temperature (K)	298.16

(vi) Retain the default values for other parameters

(c) Click **OK** to close the **Discrete Phase Model** dialog box.

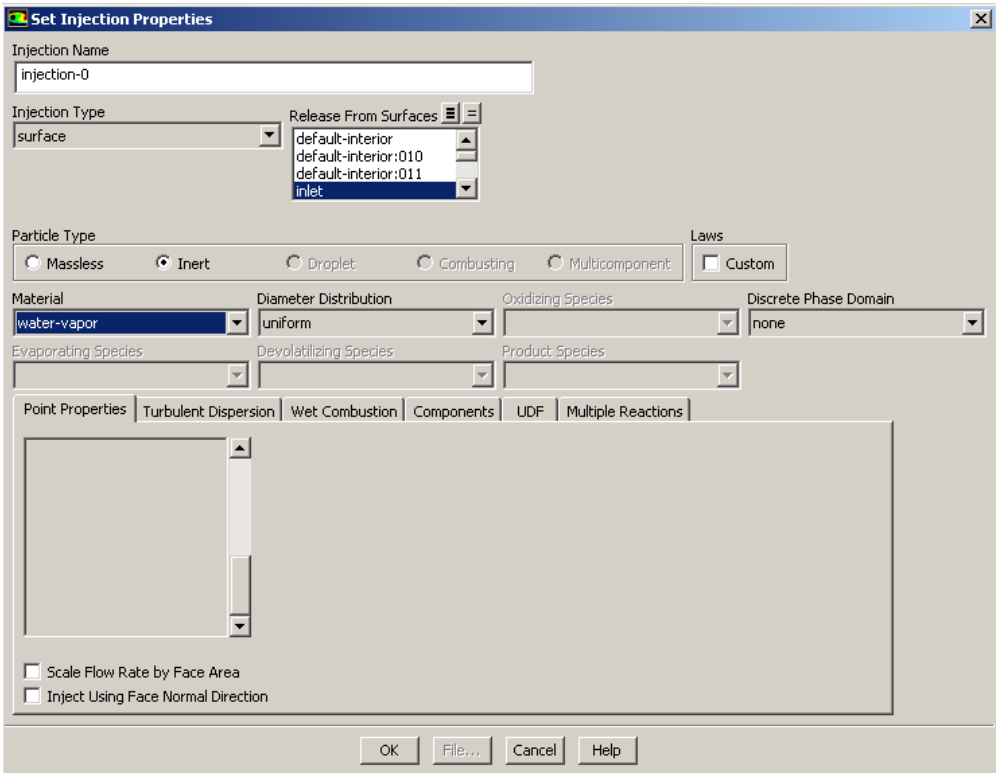

Step 4: Materials

12. Add water to the list of fluid materials and change the density of air to ideal-gas.

Materials > Fluid > Create/Edit…

(a) Copy **water-liquid** from database.
   (i) Click the FLUENT Database… to open the FLUENT Database Materials dialog box
   (ii) Select water-liquid from the FLUENT Fluid Materials list.
   (iii) Click Copy and close the Fluent Database Materials dialog box.

(b) Change the density of air to ideal-gas from the properties.
   (i) Select **ideal-gas** from the **density** drop down list

(c) Close the **Create/Edit Materials** dialog box.

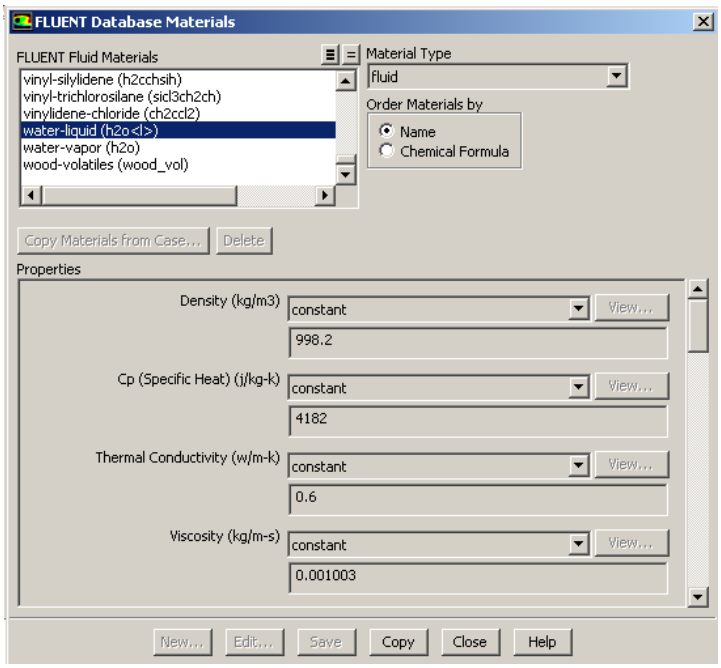

Step 5: Phases

13. Define the primary phase.

    Phase > phase-1-Primary Phase > Edit…

    (a) Enter *air* for Name
    (b) Select **air** in the **Phase Material** drop-down list.
    (c) Click **OK** to close the **Primary Phase** dialog box.

14. Define the secondary phase

    Phase > phase-1-Secondary Phase > Edit…

    (a) Enter *water-liquid* for Name
    (b) Select **water-liquid** in the **Phase Material** drop-down list.
    (c) Click **OK** to close the **Secondary Phase** dialog box.

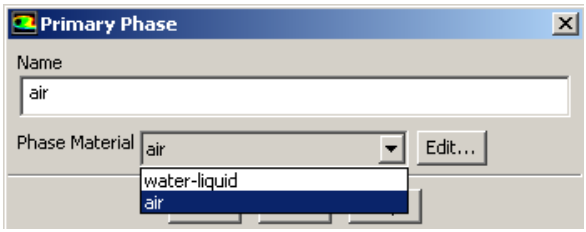

Step 6: Boundary Conditions

15. Set the boundary conditions at the inlet

Boundary Conditions > Inlet

(a) Set the boundary condition at the inlet for the mixture
   (i) Retain the default selection of **mixture** in the **phase** drop-down list.
   (ii) Click the **Edit** button to open the **Pressure Inlet** panel.
   (iii) Retain the default value of 0 for the **Gauge Total Pressure**.
   (iv) Click **OK** to close the **Pressure Inlet** Panel.

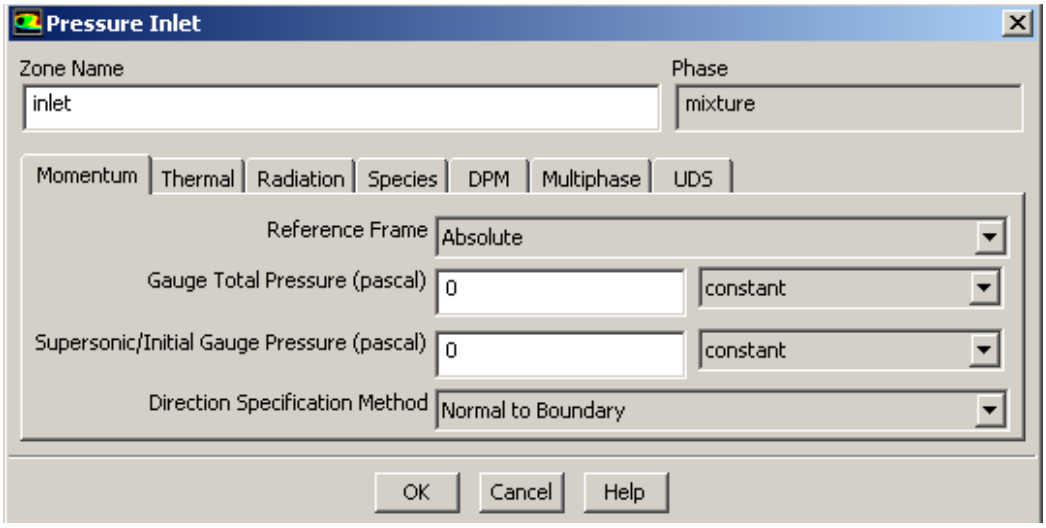

(b) Set the boundary condition at the inlet for the water-liquid
   (i) Select the **water-liquid** from the **Phase** drop-down list.
   (ii) Click the **Edit** button to open the **Pressure Inlet** panel.
   (iii) Click the **Multiphase** tab and enter 1 for the **Volume Fraction.**
   (iv) Click **OK** to close the **Pressure Inlet** panel.

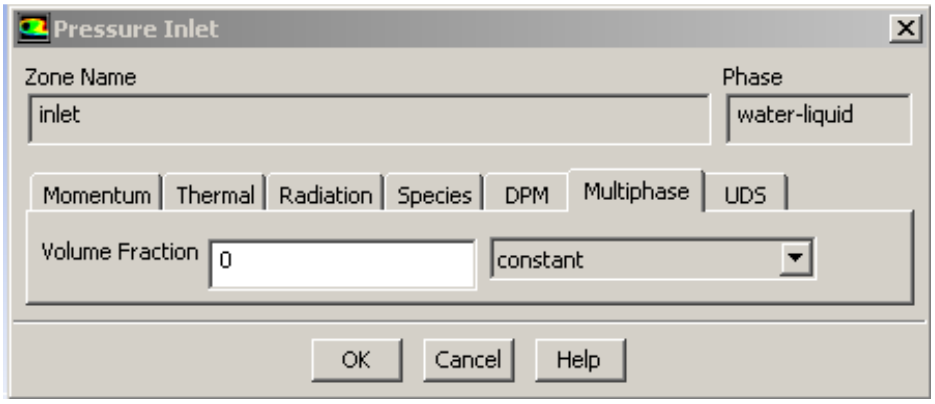

16. Set the boundary condition at the wall for the mixture
    Boundary Conditions > wall

    (a) Retain the default selection of **Mixture** in the **Phase** drop-down list.
    (b) Retain the default setting of No Slip for shear condition.
    (c) Retain the default setting of stationary wall for Wall Motion.

17. Set the porous zone for the scaffold
    Cell Zone Conditions > scaffold

    (a) Select the **water-liquid** from the **Phase** drop-down list.
    (b) Click the **Edit** button to open the **Fluid** panel.
    (c) Enable the **Porous Zone** option to activate the porous zone model.
    (d) Select the **Porous Zone** tab and enter *0.80* for **fluid porosity**.
    (e) Click **OK** to close the **fluid** panel.

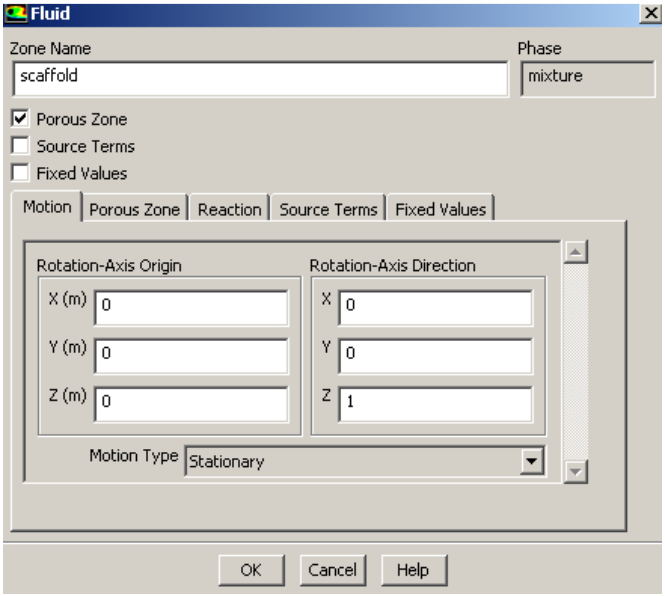

Step 7: Operating Conditions

18. Set the operating reference pressure location.
    Boundary Conditions > Operating Conditions…

    (a) Enable **Gravity**.
    (b) Enter *0.002m* for **X**.
    (c) Enter 0 for Y.
    (d) Enter *-0.0005m* for **Z**.
    (e) Set the **Gravitational Acceleration** in the **Z** direction to *-9.81 m/s*^{2}.

(f) Enable the **Specific Operating Density** and retain the value of *1.225 kg/m*^{3} for the **Operating Density.**
(g) Click **Ok** to close the **Operating Conditions** dialog box.

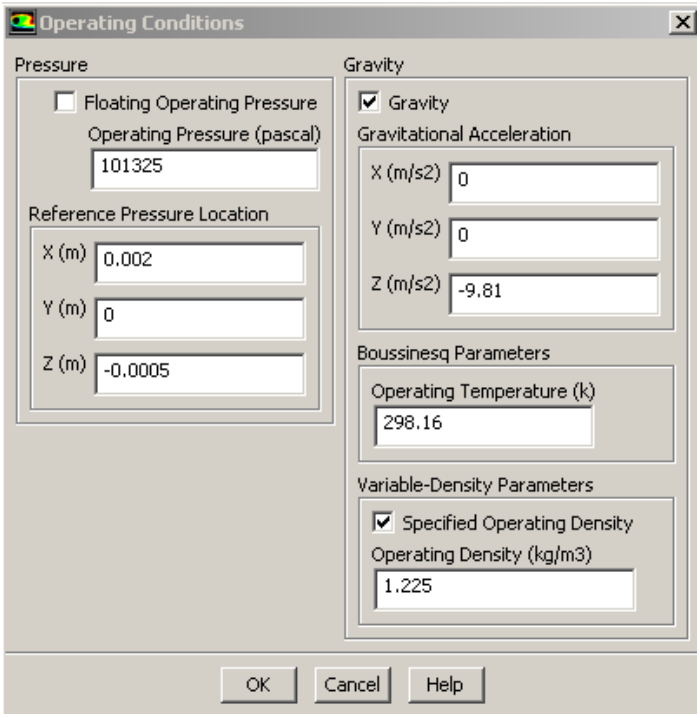

Step 8: Solution

19. Set the solution method parameters.

Solution Methods

(a) Retain the selection of **First Order Implicit** from the **Transient Formulation** drop-down list.
(b) Select **SIMPLE** from the Scheme drop-down list in **Pressure-Velocity Coupling** group box.
(c) Select **Green-Gauss Node Base**d from the **Gradient** drop-down list.
(d) Select **PRESTO!** from the **Pressure** drop-down list in the **Spatial Discretization** group box.
(e) Select **Second Order Upwind** for **Momentum** and **Density**.
(f) Select **CICSAM** for **volume fraction**.
(g) Retain the selection of **First Order Implicit** for **Energy**.

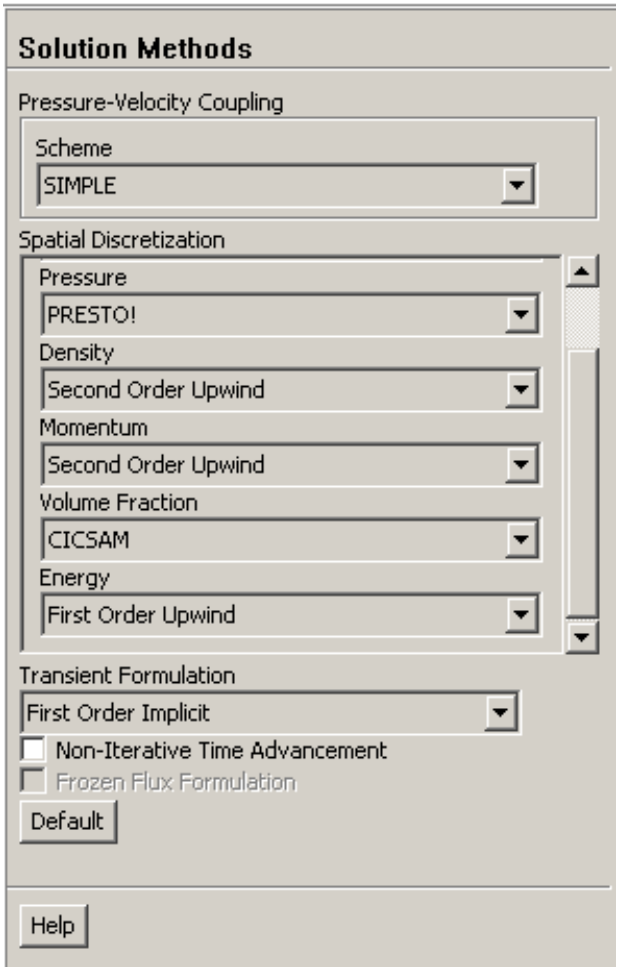

20. Click Initialize to initialize the flow field

Solution Initialization

(a) Retain the default setting for all the parameters.
(b) Click **Initialize** and close the Solution Initialization panel.

21. Create an adaption register for patching

Adapt > Region…

(a) Define a register for the air-tight cavity.

(i) Retain **Hex** from the **Shapes** list

(ii) Set up the **Input Coordinates** as shown in the following table:

Input Coordinates	Values
(X Min, X Max)	(0, 0.0165)
(Y Min, Y Max)	(0, 0.0165)
(Z Min, Z Max)	(-0.009, 0)

(b) Define the register for the tip of the needle.

(i) Enable **Cylinder** from the **Shapes** list

(ii) Set up the **Input Coordinates** as shown in the following table:

Input Coordinates	Values
(X Min, X Max)	(0, 0)
(Y Min, Y Max)	(0, 0)
(Z Min, Z Max)	(0, 0.001)
Radius (m)	0.000419

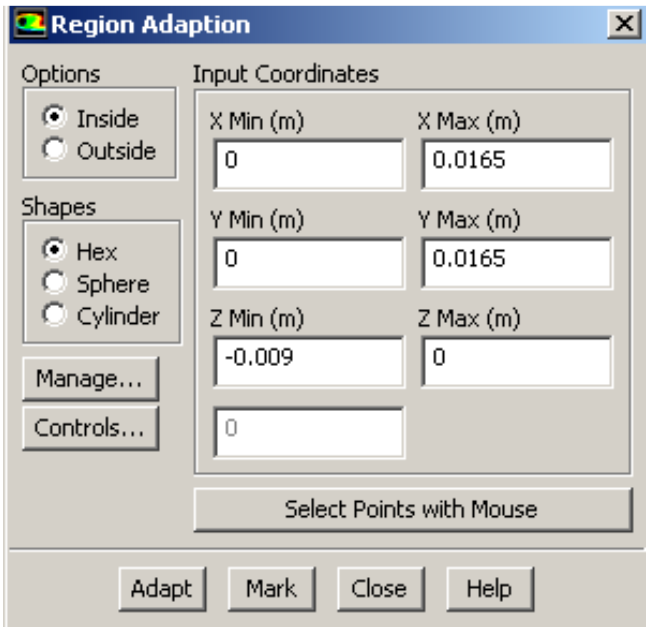

22. Patch the liquid volume fraction and initial vacuum pressure.

Solution Initialization > Patch…

(a) Select **liquid-water** from the **Phase** drop-down list.
(b) Select **Volume Fraction** from the **Variable** list.
(c) Enter **1** for **Value**.

(d) Select **cylinder-r1** from the **Registers to Patch** list.
(e) Click **Patch**
(f) Select **Mixture** from the **Phase** drop-down list.
(g) Select **Pressure** from the **Variable** list.
(h) Enter **-100,000** for **Value**.
(i) Select **hexahedron-r0** from the **Register to Patch** list.
(j) Click **Patch** and close the **Patch** dialogue box.

23. Enable the plotting of the residuals.

Monitor > Residuals > Edit…

(a) Disable **Check Convergence** for **continuity, x-velocity, y-velocity, z-velocity** and **energy** equation from **Equations** drop-down list.
(b) Click **Ok** to close the **Residual Monitors** dialog box.

24. Enable the autosave every 500 time step.

Calculation Activities

(a) Enter 500 for **Autosave Every** (Time Step).
(b) Click **Edit**… to open the **Autosave** dialog box.
(c) Enter an appropriate **File Name** (100k.dat.gz).
(d) Select **Flow-Time** from **Append File Name with** drop-down list.
(e) Click **OK** to close the **Autosave** dialog box.

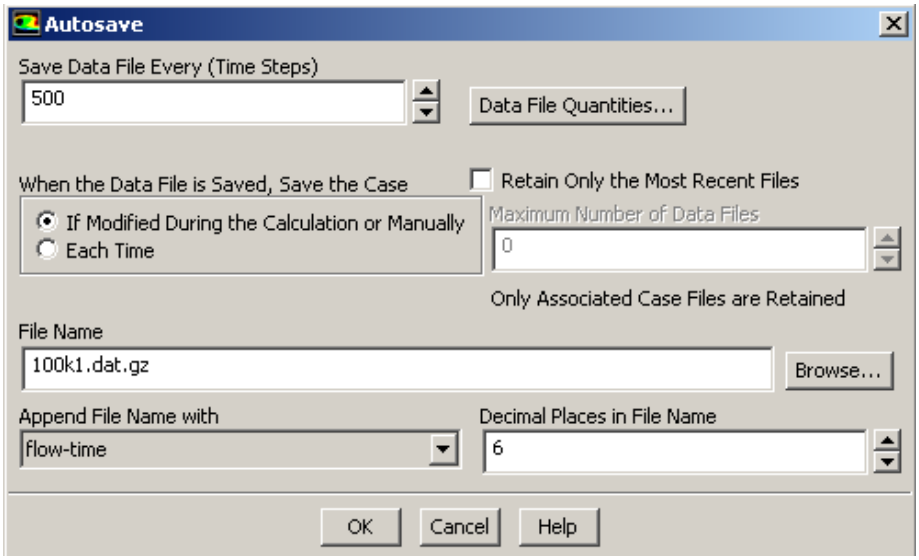

25. Calculate the solution.

Run Calculation

(a) Select **Variable** from the **Time Stepping Method** list.
(b) Enter *1e-05* for **Time Step Size** and *200,000* for **Number of Time Steps**.
(c) Click **Settings…** to open **Variable Time Settings** dialog box.
    (i) Enter *2* for **Ending Time**.
    (ii) Enter *1e -06* and *0.05* for **Minimum Time Step Size** and **Maximum Time Step Size**, respectively.
    (iii) Retain the default **Maximum Step Change Factor**.
    (iv) Click **Ok**
(d) Save the case and data files (100k.cas/dat.gz)
(e) Click **Calculate.**

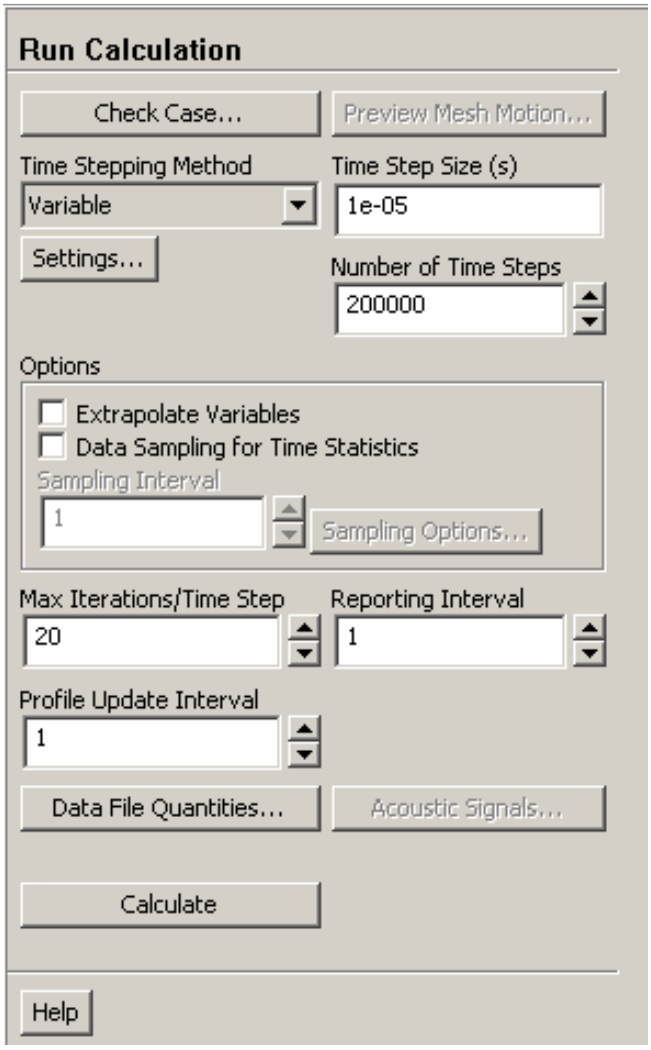

Step 9: Post Processing

26. Read the data file for the solution after 0.0001 seconds.

    File > Read > Data…

27. Create hardcopy files for animation.

    File > Save Picture…

    (a) Select **TIFF** from the **Format** list.
    (b) Select **Colo**r from **Coloring** list and click **Apply**.
    (c) Close Save **Picture** dialog box.

28. Create Surfaces from the scaffold and fluid zone.

    Surface > Zone…

    (a) Select **Fluid** from the **Zone** list and enter *fluid-surface* for the **New Surface Name**.
    (b) Click **Create.**
    (c) Select **Scaffold** from the **Zone** list and enter *Scaffold-surface* for the **New Surface Name**.
    (d) Click **Create.**
    (e) Close the **Zone Surface** dialog box.

29. Create an iso-surface for volume fraction for liquid-water in scaffold zone and fluid zone.

    Surface > Iso-Surface…

    (a) Select **Phases…** and **Volume fraction** from **Surface of Constant** drop-down lists.
    (b) Select **Water-liquid** from the **Phase** drop-down lists.
    (c) Select **Fluid** from the **From Zone** drop-down lists.
    (d) Enter *0.5* for **Iso-Values** and **vf05-fluid** for the **New Surface Name**.
    (e) Click **Create**
    (f) Select **Scaffold** from the From **Zone** drop-down lists.
    (g) Enter *0.5* for **Iso-Values** and **vf05-scaffold** for the **New Surface Name**.
    (h) Click **Create** and close the **Iso-Surface** dialog box.

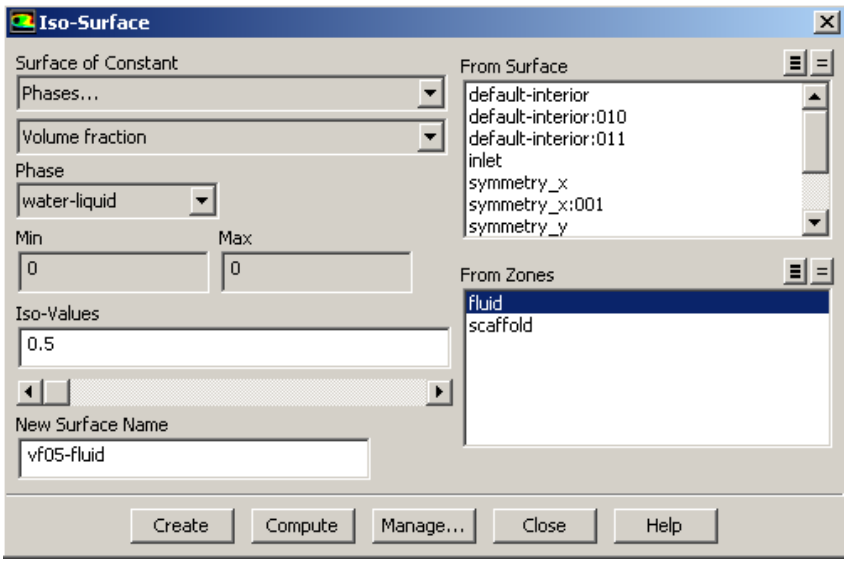

30. Clip the fluid-surface and scaffold-surface to the values of volume fraction of water-liquid between 0.5 and 1.

    Surface > Iso-Clip…

    (a) Select **Phases …** and **Volume fraction** from the **Clip to Value** of drop-down lists.
    (b) Select **liquid-water** from the **Phase** drop-down list.
    (c) Select **Fluid-surface** from **Clip Surface** list.
    (d) Enter *0.5* and *1* for **Min** and **Max,** respectively.
    (e) Enter **Clipf05-fluid** for the **New Surface Name**.
    (f) Click **Clip**.
    (g) Select **Scaffold-surface** from **Clip Surface** list.
    (h) Enter **Clip05-scaffold** for the **New Surface Name.**
    (i) Click **Clip** and close the **Iso-Clip** dialog box.

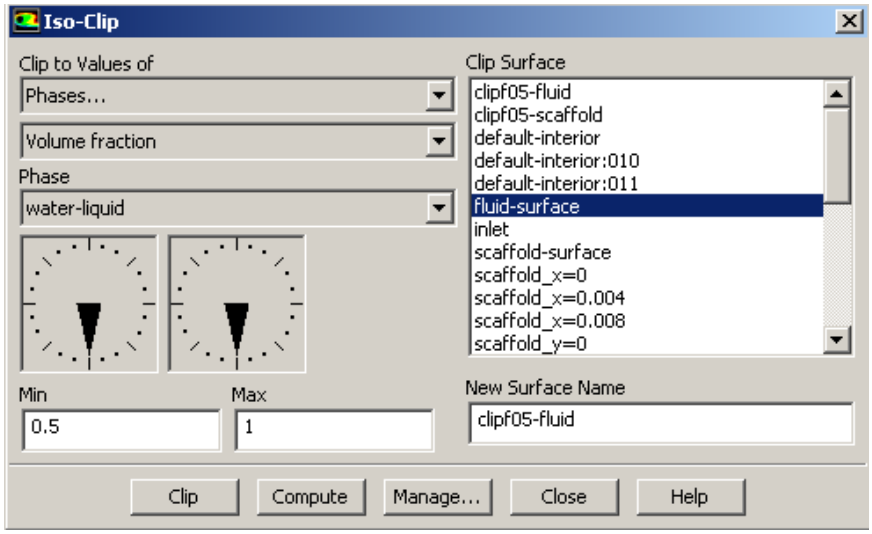

31. Display the mesh.

    Graphics and Animations > Mesh > Set-Up…

    (a) Disable **Edges** from the **Options** group box.
    (b) Enable **Faces** from the **Options** group box.
    (c) Deselect all the surfaces.
    (d) Select **clip05-scaffold, clip05-fluid, vf05-fluid, vf05-scaffold** and **wall** from the **Surfaces** lists.
    (e) Click **Display** and Close the **Mesh Display** dialog box.

32. Manipulate the Display using the Scene Description dialog box.

    Graphics and Animations > Scene…

    (a) Select **clipf05-fluid** and **vf05-fluid** from the Names list.
    (b) Click **Display…** in the **Geometry Attributes** group box to open the **Display Properties** dialog box.
    (c) Set the sliders for Red, Green and Blue to *255, 0, 0,* respectively, in the **Color** group box.
    (d) Enable **Lighting** in the **Visibility** group box.
    (e)Disable **Edges, Lines,** and **Nodes** in the **Visibility** group box.
    (f) Enable **Outer Faces** in the **Visibility** group box.
    (g) Click **Apply** and close the **Display Properties** dialog box.
    (h) Repeat for **clip05-scaffold** and **vf05-scaffold** from the **Names** list. (Set slider to 0, 0, 225)
    (i) Select **Inlet** and **Wall** in the Names list.

(j) Click **Display…** in the **Geometry Attributes** group box to open the **Display Properties** dialog box.
(k) Set the slider for **Transparency** to *71*.
(l) Set the sliders for Red, Green and Blue to *255, 255, 255,* respectively, in the Color group box.
(m) Repeat (d) to (g)
(n) Close the **Scene Description** dialog box.

33. Write a journal file to save hardcopy files of each saved time points.

File > Write > Start Journal…

(a) Display Mesh (see 31)
(b) Enable **Light On** and **Headlight On.**

Graphics and Animations > Lights…

(c) Create a hardcopy of the fluid interface.

File > Save Picture…

(d) Click **Save…** button to open the **Select File** dialog box.
(e) Enter *100k-image-%t.tif*
(f) Stop writing the journal

File > Write > Stop Journal…